Theses and Dissertations

1-1-2013

Development of High-Throughput Catalyst Screening For Ammonia Based Selective Catalytic Reduction of Nitric Oxide With Parallel Analysis Using Fourier Transform Infrared Imaging

Shahriar Salim
University of South Carolina - Columbia

Follow this and additional works at: http://scholarcommons.sc.edu/etd

Recommended Citation

Salim, S.(2013). *Development of High-Throughput Catalyst Screening For Ammonia Based Selective Catalytic Reduction of Nitric Oxide With Parallel Analysis Using Fourier Transform Infrared Imaging.* (Master's thesis). Retrieved from http://scholarcommons.sc.edu/etd/2448

Development of High-Throughput Catalyst Screening for Ammonia Based Selective Catalytic Reduction of Nitric Oxide with Parallel Analysis Using Fourier Transform Infrared Imaging

by

SHAHRIAR SALIM

Bachelor of Science

Bangladesh University of Engineering and Technology, 2008

_____

Submitted in Partial Fulfillment of the Requirements

For the Degree of Master of Science in

Chemical Engineering

College of Engineering and Computing

University of South Carolina

2013

Accepted by:

Anton J. Lauterbach, Director of Thesis

John W. Weidner, Chair, Reader

Jason Hattrick-Simpers, Reader

Jamil Khan, Reader

Lacy Ford, Vice Provost and Dean of Graduate Studies

ABSTRACT

Lean-burn engines, which operate under excess air to fuel ratio offer significant fuel efficiency as well as contribute to the reductions of greenhouse gas emissions. However, lean burn engines produce three main pollutants carbon monoxide (CO), nitrogen oxides (NO_x) and unburned or partially burned hydrocarbons (HC), which have detrimental effect on both environment and human life. The conventional three way catalyst (TWC) which was designed to reduce NO_x under stoichiometric conditions is not effective under lean-burn engine exhaust condition. Recent studies have shown that copper (Cu) exchanged chabazite (CHA) type zeolites are very promising catalysts for urea or ammonia (NH_3) based selective catalytic reduction (SCR) of NO_x and expected to meet with our future needs, due to their low temperature activity and high hydrothermal stability.

High-throughput experimentation (HTE) is an active area of interest in the field of catalysis due to its potential in optimization of time and cost. Fourier transform infrared (FTIR) imaging is a powerful spectroscopic tool which combines the chemical sensitivity of infrared spectroscopy with the ability to rapidly analyze multiple samples simultaneously. A large number of heterogeneous catalysts can be tested under realistic condition using a high-throughput parallel reactor (HTR) and the product gases can be analyzed quantitatively in parallel simultaneously using FTIR imaging technique.

iii

The objective of this research is to develop high-throughput catalyst screening for NH_3 based SCR of NO_x. High throughput methodology (HTM) will allow us to perform a significant number of experiments in a short period of time and will be beneficial for comparison of activity and selectivity of a significant number of catalysts.

The first chapter of the thesis summarizes the motivation as well as the present NO_x reduction methods and limitations of those methods. It also summarizes the progresses of HTM for parallel testing of catalysts under realistic conditions.

The second chapter provides the detail of the 16 channel HTRs (Primary and Secondary screening reactor) used to test the 16 powdered catalysts under plug flow condition. It also provides the detail of FTIR imaging system built for the parallel analysis of the reaction product gases. A brief description of chemometrics for quantitative infrared spectral analysis is also included. Lastly, this chapter summarizes the catalyst synthesis and characterization techniques used in this research.

The third chapter details the experimental results of CO oxidation reaction. It summarizes the calibration results of CO and carbon dioxide (CO_2). It also provides the results of catalyst screening for CO oxidation reaction using the primary screening reactor (PSR) along with the results of characterization of catalysts used to study CO oxidation reaction.

The fourth chapter details the experimental results of NH_3 based SCR of nitric oxide (NO). It summarizes the univariate and multivariate calibration results used for NH_3 based SCR reaction study. It also provides the results of benchmark reaction and catalyst screening using the secondary screening reactor (SSR).

The last chapter provides a perspective of this research and recommendations for the direction of future works.

TABLE OF CONTENTS

LIST OF TABLES

LIST OF FIGURES

CHAPTER 1

Introduction and background

1.1. Motivation

Air pollution caused by automobile engines is an issue of general interest. Automobile engines employ combustion of fossil fuels as a source of energy. Burning of hydrocarbon ideally leads to the generation of water (H_2O) and CO_2. However, due to incomplete combustion and high temperatures reached in the combustion chamber, the automobile engines exhaust contains significant amounts of pollutants [1-4]. Three primary pollutants of exhaust gas are CO, NO_x and HC. NO_x (NO and NO_2) exhaust is a major threat to the environment because they are responsible for photochemical smog formation, acid rain, ozone generation in the low troposphere, and ozone layer depletion in the stratosphere [5]. Biological studies have shown that, when externally produced NO is introduced to the lungs the compound can diffuse through the alveolar-cells and capillary vessels provoking both lung infections and respiratory allergies like bronchitis, pneumonia, etc. [2]. Figure-1.1 shows the percentage of NO_x pollution by source in the United States in 2010. According to the emissions inventory taken by the U.S. Environmental Protection Agency (EPA) in 2010, 55.37% of the total NO_x emissions released into the atmosphere originated from mobile sources as shown in Figure-1.1.
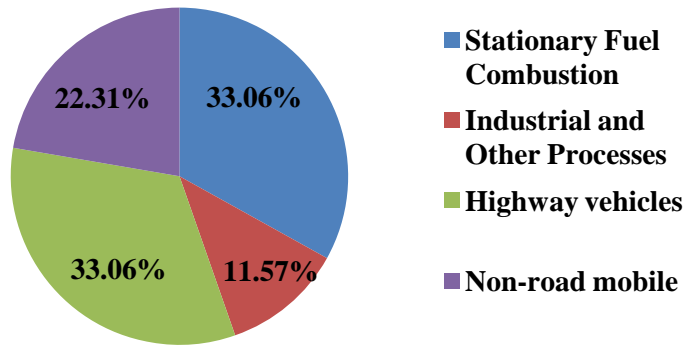
Figure-1.1: Distribution of national NO$_x$ emission by source in the USA, 2010 [6].

Growing public concerns about deteriorating air quality prompted the passages of United States Clean Air Act in 1970. This led to the discovery of the TWC in 1979, which is still found in virtually all modern catalytic converters. The TWC uses a combination of noble metals platinum (Pt), palladium (Pd) and rhodium (Rh) supported on aluminum oxide (Al$_2$O$_3$) in order to oxidize CO and unburned HC to CO$_2$ and reduce NO$_x$ to Nitrogen (N$_2$) [7]. The TWC was highly successful in controlling exhaust emissions from conventional petrol engines which operate close to stoichiometric conditions [8, 9]. Over the next two decades, TWC is modified to improve its overall durability and activity. Small amounts of other supports such as, zirconia (ZrO$_2$), ceria (CeO$_2$) and baria (BaO) were added to increase the thermal stability, oxygen (O$_2$) storage and release capacity of the catalyst surface [10]. As environmental regulation became more stringent, the improvement of catalytic converters performance becomes more important. In addition, concerns about the effect of global warming have driven the interest in reducing greenhouse gas emissions especially CO$_2$ emissions. One of the effective ways to reduce the overall emission of CO$_2$ is to reduce the fuel consumption of

vehicles. Lean-burn engines, which operate under excess air to fuel ratio, is one of the

potential solutions to reduce CO_2 emissions and simultaneously improve the overall fuel

economy. The excess O_2 helps to combust the residual CO and HC thus increasing the

fuel efficiency and decreasing the fuel consumption [11]. The exhaust gas compositions

of the engines operating under lean-burn condition are shown in Table-1.1. It is clear that;

NO_x emission from a lean burn engine is higher than from a diesel engine.

Table-1.1: Exhaust conditions of diesel and lean-four-stroke engines (reproduced from [1])

Exhaust components and conditions[a]	Diesel engine	Four-stroke lean-burn spark ignited-engine
NO_x	350–1000ppm	≈ 1200ppm
HC	50–330ppm C_1	≈ 1300ppm C_1
CO	300–1200ppm	≈1300ppm
O_2	10–15%	4–12%
H_2O	1.4–7%	12%
CO_2	7%	11%
SO_x	10–100ppm[b]	20ppm
PM	65 mg/m^3	
Temperature (test cycle)	r.t.–650°C (r.t.–420°C)	r.t.–850°C
GHSV (h^{-1})	30,000–100,000	30,000–100,000
λ (A/F)^c	≈1.8 (26)	≈1.16 (17)

[a] N_2 is remainder.

For comparison: diesel fuels with 500 ppm of sulfur produce about 20 ppm of SO_2.

λ defined as ratio of actual A/F to stoichiometric A/F, $\lambda = 1$ at stoichiometry (A/F = 14.7).

The TWC was not designed to operate under lean-burn engine exhaust condition and it cannot remove NO_x effectively under these net-oxidizing conditions [8-9, 12-14]. Therefore, new catalyst must be developed in order to reduce NO_x from lean-burn engine exhaust and to meet future requirements of EPA. Figure 1.2 shows the EPA regulation standards to date for NO_x for Compression Ignition (CI) and Spark Ignition (SI) engines. As shown in Figure-1.2, the regulations for 2008+ restrict the NO_x content to be as low as ~ 0.2 (g/bhp-hr). Extensive research has been performed in search of alternative catalysts that will reduce NO_x in O_2 rich environments, but an acceptable catalyst has not yet been discovered [12-14].
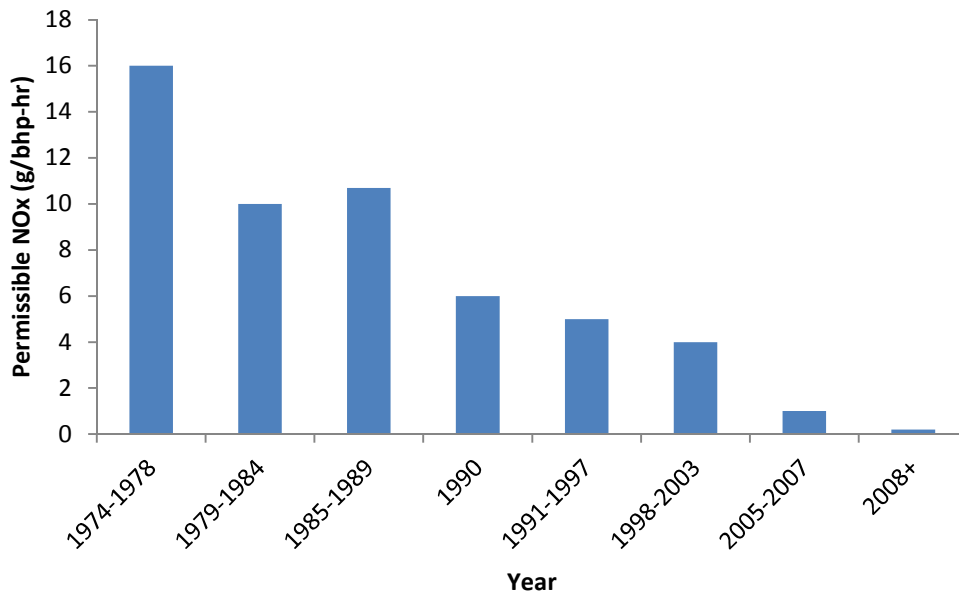
Figure-1.2: Exhaust emission standards for NO_x by EPA [15].

1.2. Existing technologies for removal of NO_x and their limitations

The NO_x emissions from automobile engine exhaust is typically 95% NO and 5% NO_2. In engine NO_x is generated through one of the three mechanisms. The mechanism that contributes mostly to automotive exhaust is thermal NO_x; which is generated from the oxidation of elemental N_2 in the air at high temperatures as shown in reaction (1.1). This reaction occurs above 1000^oC [16].

$$N_2 + O_2 \leftrightharpoons 2NO \ \dots (1.1)$$
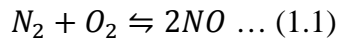
The second mechanism of NO_x formation is called fuel NO_x and is generated from the oxidation of N_2 present in the fossil fuel. Unlike thermal NO_x, the fuel NO_x formation is relatively independent of temperature at internal combustion engine temperatures [17].

The third mechanism of NO_x formation is called prompt NO_x (also called Fenimore NO). In this case HC reacts with atmospheric N_2 to yield hydrogen cyanides (HCN and H_2CN). These cyanides can be oxidized to NO in the fuel lean zone as shown in the following reactions.

$$HC + N_2 \rightarrow HCN \ \dots (1.2)$$

$$HC + N_2 \rightarrow H_2CN \ \dots (1.3)$$

$$HCN + O_2 \rightarrow NO + CO_2 + H_2O \ \dots (1.4)$$

$$H_2CN + O_2 \rightarrow NO + CO_2 + H_2O \ \dots (1.5)$$
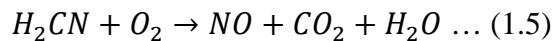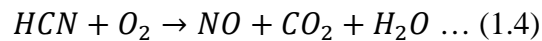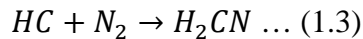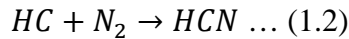
In addition, NO can further react with O_2 to form NO_2 and N_2O as shown in the following reactions [3].

$$NO + \frac{1}{2}O_2 \leftrightharpoons NO_2 \ \dots (1.6)$$

$$2NO \leftrightharpoons N_2O + \frac{1}{2}O_2 \ \dots (1.7)$$
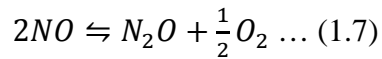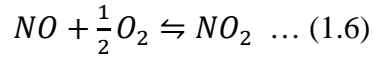
NO has a positive free energy of formation at ambient temperature. Therefore the decomposition reaction of NO is thermodynamically favorable. However, homogenous decomposition is immeasurably slow because the decomposition reaction has very high activation energy as shown in the reaction (1.8). Forcing the decomposition reaction to the right also becomes increasingly more difficult in an environment exposed to air. According to LeChatelier's principle high partial pressures of N_2 and O_2 will shift the equilibrium of the decomposition reaction to the left.

$$NO \leftrightharpoons \frac{1}{2}N_2 + \frac{1}{2}O_2 \qquad \Delta H_{298}^0 = 364kJ/mol \ \dots (1.8)$$
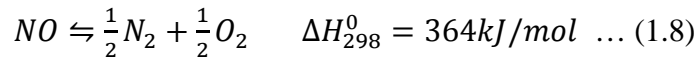
Furthermore in O_2 rich environment at moderate temperatures NO oxidizes to form NO_2. Therefore, an effective NO_x reduction catalyst which drives NO decomposition reaction to the right and inhibits NO oxidation and hence can reduce the NO_x concentration to levels that satisfy upcoming regulatory standards needs to be investigated [2].

There are two main approaches for NO_x reduction that have been used over the past several years. The first method is the NO_x storage and reduction (NSR) technology, where NO_x elimination is achieved by selectively storing NO_x on the catalyst surface under fuel lean conditions, and then non-selectively reducing the stored NO_x under short,

6

fuel rich conditions [18-26]. The second approach is the SCR of NO_x in which the catalyst and the reducing agent (e.g. NH_3, urea and hydrocarbons) react selectively with NO_x rather than with O_2. These technologies include NH_3 SCR, urea SCR and hydrocarbon SCR (HCSCR) [4].

NSR catalysts were initially developed by Toyota in the early 1990s. NSR catalysts overcome the limitations of the TWC by operating under non-steady state conditions. During fuel-lean conditions, the storage component of the NSR catalyst (most commonly BaO supported on γ-alumina (Al_2O_3)) traps the NO_x, while the oxidation component of the catalyst (typically Pt) oxidizes CO and HCs to CO_2. Eventually, the sites that trap the NO_x become saturated and are regenerated by running the engine under fuel-rich conditions where the adsorbed NO_x is reduced by HCs and released as N_2 as shown in the following reactions.

$$2CO + O_2 \rightarrow 2CO_2 \text{ ... (1.9)}$$

$$HC + O_2 \rightarrow CO_2 + H_2O \text{ ... (1.10)}$$

$$NO + HC \rightarrow N_2 + CO_2 + H_2O \text{ ... (1.11)}$$
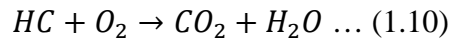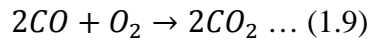
Although NSR catalysts have been successfully commercialized, there are some complications present in the use of NSR catalysts, such as a fuel penalty for the rich events, sensitivity to fuel sulfur levels, and control under transient engine operation [18-26].

HCSCR has achieved great attention in the scientific community over the past four decades. The two main reactions of HCSCR are the reduction of NO and oxidation of HC and CO as shown in the following reactions.

$$NO + HC + O_2 \rightarrow N_2 + CO_2 + H_2O \text{ ... (1.12)}$$

7

$$HC + O_2 \rightarrow CO_2 + H_2O \ \dots \ (1.13)$$

$$2CO + O_2 \rightarrow 2CO_2 \ \dots \ (1.14)$$
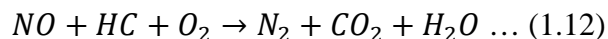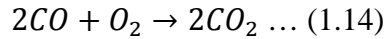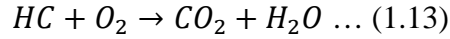
Propene (C_3H_6), propane (C_3H_8), octane (C_8H_{18}) and ethanol (C_2H_5OH) are mostly reported as the reducing agents used for HCSCR, whereas Pt on γ-Al_2O_3 (Pt/γ-Al_2O_3) and silver (Ag) on γ-Al_2O_3 (Ag/γ-Al_2O_3) are the most common catalysts [8-9, 12-14, 27-46]. Pt/γ-Al_2O_3 showed good NO_x reduction ($\sim$50%) at low temperature (200-250^{o}C) with C_3H_6. However, N_2 selectivity was low compared to nitrous oxide (N_2O) selectivity ($\sim$74%), which was not desired [8, 13-14]. On the other hand, Ag/γ-Al_2O_3 showed good NO_x reduction ($\sim$100%) at high temperature (350-500°C) with C_2H_5OH or C_8H_{18}. However, CO production (40%) was observed instead of CO conversion [9, 12, 27-29, 35-37]. To increase the temperature range and CO_2 selectivity some steps have been taken, such as injecting H_2 and using an oxidation cleanup catalyst. It was found that oxidation catalyst increased the conversion of CO, but reduced the conversion of NO_x (40%) at 350°C [8]. H_2 injection in exhaust gas increased the NO_x reduction and CO oxidation [19]. However it is not a practical solution to add H_2 to exhaust gas. Therefore, a good solution has not been found yet [8, 12, 31-34].

To reduce NO_x emissions from the lean exhaust of stationary plants NH_3 was first used in Japan in 1970s [47-48]. This process is still regarded as the most effective method for NO_x reduction in stationary applications. However, in automotive applications NH_3 presents a risk for being transported in pressurized containers because of its toxic and corrosive nature. Therefore, SCR process with urea is presently considered to be the best technology for the removal of NO_x from the exhaust of heavy-duty diesel vehicles, e.g. trucks [3-4, 28, 47-54]. Urea is harmless and environmentally storage compound for NH_3.

Urea is usually introduced to the exhaust stream as a solution 32.5% by weight with H_2O. In exhaust stream, at high temperature urea decomposes and form NH_3. The complete decomposition of urea takes place in three steps. In first step H_2O is evaporated. In the second step urea decomposes to release one NH_3 molecule and one isocyanic acid (HNCO) molecule. Finally HNCO decomposes to release a second NH_3 molecule and one CO_2 molecule as shown in the following reactions.

$$NH_2CONH_2 \rightarrow NH_3 + HCNO \ \dots \ (1.15)$$

$$HCNO + H_2O \rightarrow NH_3 + CO_2 \ \dots \ (1.16)$$
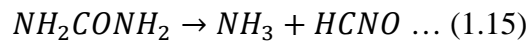
Although urea or NH_3 SCR is a mature technology, there are still some complications, such as NH_3 slip through the exhaust, formation of ammonium sulfates (NH_4HSO_4, $(NH_4)_2SO_4$) on SCR catalyst surface below 250^oC and cold weather freezing. The urea solution freezes at -11^oC and expands by approximately 7% when frozen [3, 49-51]. If urea solution freezes when the vehicle is shut down, startup is not inhibited. The SCR heating system is designed to quickly return the urea solution to liquid form so that the operation of the vehicle is not effected. The NO reduction efficiency of this process is 90% or even higher [4].

The basic reaction of urea or NH_3 SCR is the reduction of NO by NH_3 in presence of O_2. In case of incomplete decomposition of urea, urea and HCNO can also act as a reducing agent as shown in the following reactions [52].

$$4NO + 4NH_3 + O_2 \rightarrow 4N_2 + 6H_2O \ \dots \ (1.17)$$

$$2NO + 6NH_2CONH_2 \rightarrow 5N_2 + 4H_2O + 2CO_2 \ \dots \ (1.18)$$

$$4NO + 6HCNO \rightarrow 5N_2 + 2H_2O + 4CO_2 \ \dots \ (1.19)$$
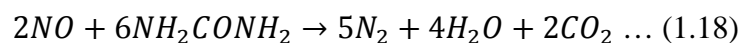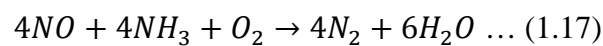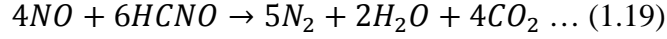
It is observed that, reaction (1.17) proceeds faster in the presence of a 1:1 mixture of NO and NO_2 (designated as fast SCR), since NO_2 is a much stronger oxidizing agent than O_2 as shown in the reaction (1.20).

$$4NH_3 + 2NO + 2NO_2 \rightarrow 4N_2 + 6H_2O \ \dots \ (1.20)$$
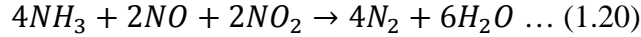
When NO_2/NO_x fraction exceeds 50%, a SCR reaction with pure NO_2 takes place as shown in the reaction (1.21) [3-4].

$$8NH_3 + 6NO_2 \rightarrow 7N_2 + 12H_2O \ \dots \ (1.21)$$
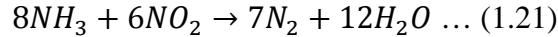
Vanadia-tungsta-titania (titania-vanadia) catalysts are widely used in the treatment of flue gases produced by stationary power plants. Vanadium oxide (V_2O_5) (0.5-1%) is the active species in the SCR process. High surface area anatase titania (TiO_2) (70–100m^2/g) constitutes the support of the catalyst. Tungsta (WO_3) (~10%) works as a physical and chemical promoter inhibiting rutilization of anatase phase of titania. Due to its high potential of NO_x reduction in lean exhaust gases, titania-vanadia is rigorously investigated for automotive applications [3-4, 55-58]. The challenges for the automotive application of urea SCR is the need of a titania-vanadia catalyst with high SCR activity and good thermal stability in the temperature range of 150–650°C. Anatase sintering and anatase-to-rutile phase transition are the major factors contributing to the deactivation of titania-vanadia catalysts above 500°C. This phenomenon decreases the catalyst surface area and results the lower activity of the rutile-based catalysts. Over 690°C, melting of V_2O_5 also contribute to the deactivation of the catalyst. Moreover volatility of V_2O_5 over 650°C can lead to toxic emission which is not desired [3-4, 55].

In addition to titania-vanadia catalyst, zeolites are promising catalysts for automobile applications due to their lower price, nontoxicity, high activity and selectivity to N_2. Zeolite types with narrow pores, such as zeolite beta (BEA), CHA, faujasite (FAU), mordenite (MOR) and mordenite framework inverted (MFI) have proved to be good NO_x reduction catalyst for NH_3 SCR applications. In particular, metal (e.g. Cu and iron (Fe)) exchanged MFI zeolite systems (Cu-ZSM-5 and Fe-ZSM-5) have received much attention both from academia and industry as good NO_x reduction catalysts [3-4, 50, 53, 59-64]. The main drawback of zeolite catalysts is its lack of hydrothermal stability. At high temperatures and in the presence of water vapor (steam), zeolite framework is compromised; combined effects of dealumination and migration of ions into framework diminishes the SCR capability [59-62]. However, recent studies have shown that CHA type zeolites (SSZ-13 and SAPO-34) are hydrothermally stable and promising catalysts for NH_3 SCR applications [3, 50, 53, 65-68]. Hydrothermal stability of a zeolite can be observed by comparing the SEM images of the zeolite before and after hydrothermal treatment as shown in Figure-1.3. Before hydrothermal treatment Cu-ZSM-5 crystals were fairly smooth and uniformly shaped as shown in Figure-1.3a. However, after hydrothermal treatment Cu-ZSM-5 loses its crystallinity as shown in Figure-1.3b. On the other hand, Cu-SSZ-13 maintains the same hexagonal morphology and surface texture before and after hydrothermal treatment as shown in Figure-1.3c and d [53].
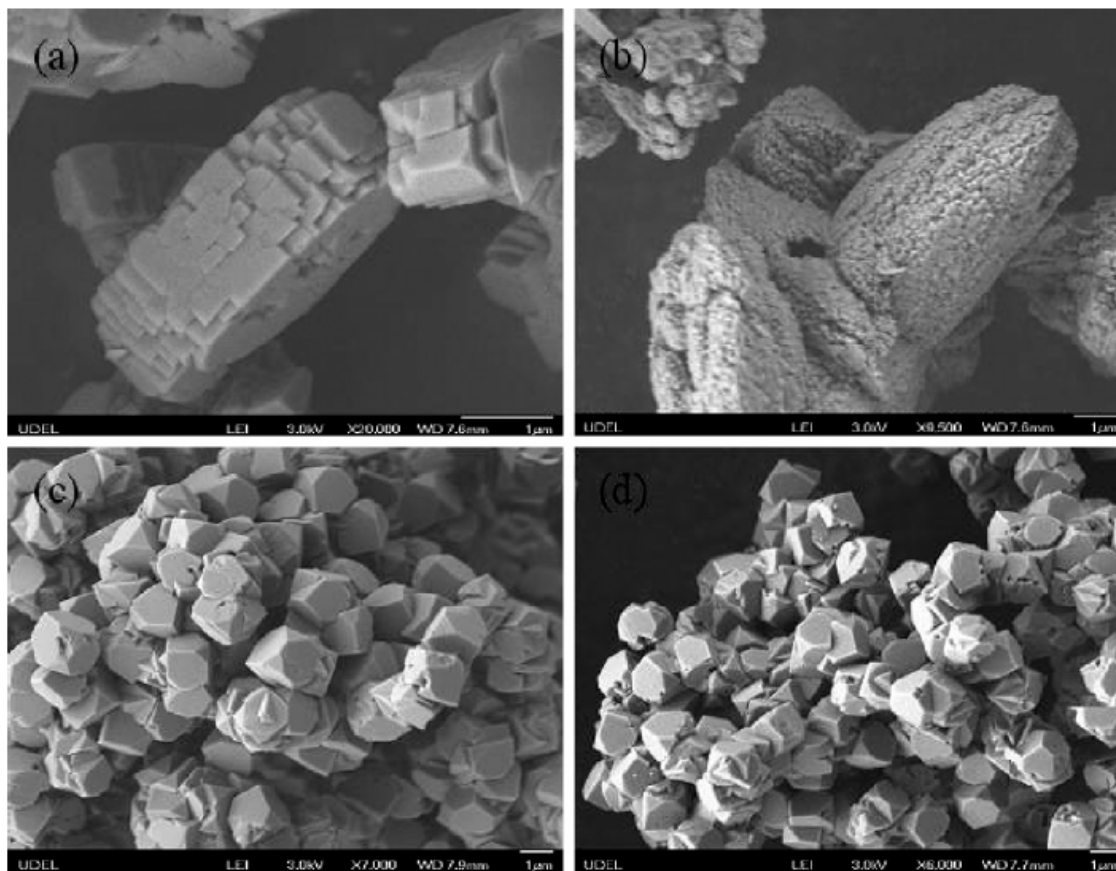
Figure-1.3: SEM images of Cu-ZSM-5 (a, b) and Cu-SSZ-13 (c, d) before and after hydrothermal treatment (Reproduced from [53]).

The NO_x reduction capability of Cu-ZSM-5, Cu-SSZ-13 and Cu-SAPO-34 are shown in Figure-1.4 after 14h of hydrothermal treatment. From Figure-1.4, it is evident that, after hydrothermal treatment NO_x reduction capability of Cu-ZSM-5 was diminished, whereas Cu-SSZ-13 and Cu-SAPO-34 still showed good NO_x reduction capability. This is because of the dealumination of the MFI framework. During hydrothermal treatment, aluminum hydroxide moiety ($Al(OH)_3$) exits the MFI framework causing structural defects which results in the reduced NO_x reduction capability. On the other hand, $Al(OH)_3$ cannot exit the small pore window of CHA framework resulting similar NO_x reduction capability before and after hydrothermal treatment. Hence, metal

exchanged CHA type zeolites (SSZ-13 and SAPO-34) are promising catalysts for NH_3 SCR applications and expected to meet with our future needs.
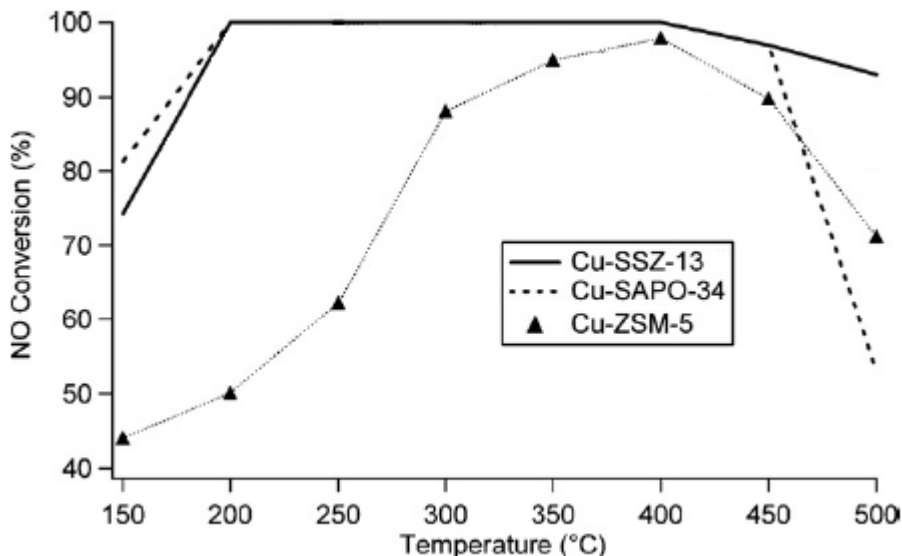
Figure-1.4: NH$_3$ SCR activity of Cu-SSZ-13, Cu-SAPO-34 and Cu-ZSM-5 after 14h hydrothermal treatment (Reproduced from [53]).

Cu and Fe promoted zeolites are most widely studied for NH_3 SCR, owing to their availability and high activity. A possible reason Cu and Fe to show high NO_x reduction is their good redox capacity. Noble metals (Pt, Pd, Rh) have higher redox capacity, but zeolites promoted with noble metals form N_2O as shown in the reactions below. Cu-ZSM-5 and Fe-ZSM-5 also produce N_2O (Cu-ZSM-5 produces more than Fe-ZSM-5). However, amount of N_2O produced by Cu-ZSM-5 and Fe-ZSM-5 is much lower compared to zeolites promoted with noble metals.

$$2NH_3 + 2NO_2 \rightarrow N_2O + N_2 + 3H_2O \ \dots \ (1.22)$$

$$6NH_3 + 8NO_2 \rightarrow 7N_2O + 9H_2O \ \dots \ (1.23)$$
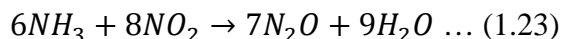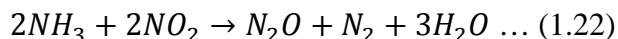
In this research metal promoted BEA, MFI and CHA type zeolites were studied for NH_3 based SCR of NO_x using NO and NH_3 conversion and N_2O selectivity.

1.3. Necessity of high-throughput experimentation

High-throughput experiment is the exploration of a wide parameter space by systematic variation of all single parameters of interest. A large number of parameters influence the performance of SCR catalysts which can be broadly classified into two categories: catalyst composition and synthesis methods and reaction conditions. The performance of SCR catalysts is strongly influenced by the catalyst composition and synthesis methods, e.g., types of support (metal oxide or zeolite), types of metal and weight loadings of metal present in the catalyst, preparation method (incipient wetness impregnation, ion exchange, etc.), calcination time and temperature, etc. In addition, reaction conditions like temperature, NO_x concentration, O_2 concentration, reducing agent concentration, space velocity and the presence of H_2O also have significant effect on the performance of SCR catalysts. Therefore, the performance study of SCR catalyst is a thorough understanding of the effect of catalyst composition and synthesis methods change as well as the effect of the reaction conditions change. This complex dependence of SCR catalytic performance on such a large number of parameters makes it difficult to do a comprehensive study of them and creates an exciting platform for the use of HTE techniques. HTE promotes rapid preparation, parallel testing and high-capacity information processing to speed up the search for new materials and understanding of fundamental scientific processes. It is an excellent technique for exploring the vast parameter space. It evaluates the performance of a significant number of catalysts simultaneously, predicts the design of new catalysts based on the extracted knowledge

and optimizes the catalyst efficiently and reduces the time to commercialization. Figure-1.5 shows the experimental strategy for HTE [11, 69]. As shown in Figure-1.5, HTE is a loop that begins with the synthesis of large libraries of potential catalyst, followed by pre reaction catalyst characterization, performance evaluation of the catalysts, post reaction catalyst characterization and predicting the design of a new catalyst based on the results of catalyst characterization and performance evaluation. This loop continues until a promising catalyst is found.
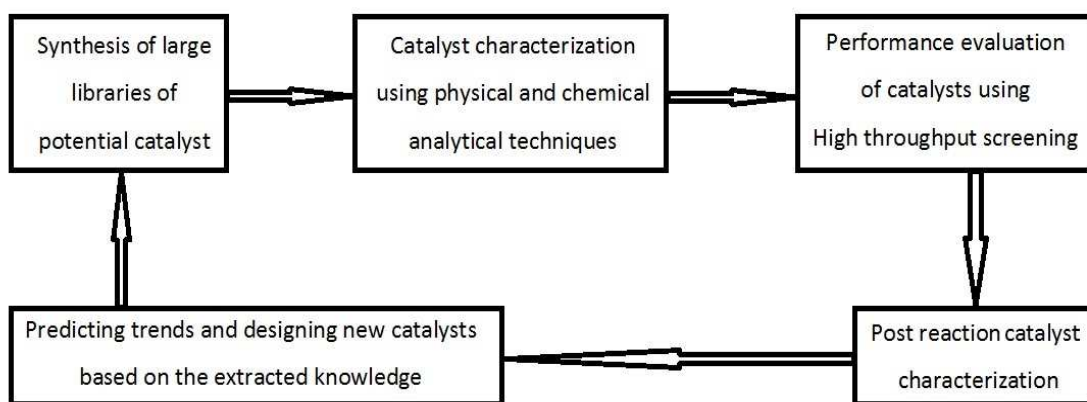
Figure-1.5: Steps of high-throughput experimentation.

The application of HTM to heterogeneous catalysis advances through three different stages: primary, secondary and tertiary screening. In primary screening, multiple libraries of materials that can perform a desired catalytic transformation are qualitatively evaluated. Libraries that do not work are eliminated in order to focus on new classes of promising materials called hits. Successful primary screens may include thousands of experiments and exploration of a broad experimental space. Hits from primary screening are evaluated further in secondary screening, which assess the viability of hits as potential

candidates. At this stage, catalysts synthetic methods and screening technologies employed closely mimic the relevant commercial processes for the purpose of comparing activity and selectivity of the potential catalysts with respect to commercial catalysts. Finally, optimized leads enter the third stage of development: tertiary screening. It includes scale-up and commercial testing of catalysts in pilot or micro plants. The goal of this stage is to scale up of the catalysts with the greatest probability of success. This greatly reduces the number of costly pilot plant runs required [70].

In HTE catalyst libraries are investigated by serial or parallel analytical technique. The most popular analytical technique is the scanning mass spectrometry which is based on rapidly analyzing the gases from one sample in a catalyst library at a time, in a sequential manner. Another high-throughput experimental method is based on photoionization of reaction products using tunable UV lasers, known as REMPI (Resonance Enhanced Multi Photon Ionization). The disadvantage of this technique is that a suitable laser frequency for each species of interest must be known and accessible. In general, the main limitation of these techniques is that the screening time is proportional to the library size. On the other hand, parallel analytical technique gathers information simultaneously from all the elements in a library. FTIR imaging is a chemically sensitive analytical technique that can analyze all library elements simultaneously. Our group has pioneered infrared spectral imaging for the rapid HTE analysis [69, 71-76].

HTE is practiced by a wide variety of industrial laboratories, e.g. Symyx, General Electric, DuPont, BASF, Chemspeed, Avantium, 3M, Bayer, Tecan, Zymark, UOP and others [76]. A HTR system, built in house (described in chapter-2) with FTIR imaging

system has proved efficient for the development of NSR catalyst [5, 7, 11, 69], screening of Ru-based NH_3 decomposition catalysts [77] and screening of catalysts for cracking of military aviation fuel [78].

1.4. Research Objectives

Two HTR systems were studied in this research. The objective of the small 16 channel parallel HTR (PSR) study was to understand the design criteria of a HTR system for practical application. The goal was to extract knowledge for preparing a HTR system devoid of crosstalk and back mixing of product gas, based on the experiments performed in the PSR. The main objective of the big 16 channel parallel HTR (SSR) study was to evaluate the performance of metal promoted zeolites for NH_3 based SCR of NO. The target was to run the reaction between the reaction temperatures of 150^oC-550^oC. Additionally a hydrothermal treatment was performed at ~750^oC in SSR to investigate the dealumination of the catalysts. In HT screening, operating conditions of each reactor should be similar to each other in order to compare the performances of the catalysts reliably. A lot of efforts have been performed to make sure each reactor shows the same activity within the experimental error.

CHAPTER 2

Experimental Setup

2.1. Introduction

Reactor systems and analytical techniques used for the experiments, catalyst preparation, performance evaluation and characterization are discussed in detail in this chapter. Two HTR systems were used for NH_3 SCR of NO experiments. PSR was initially used to test the CO oxidation reaction. However, the main studies were performed using SSR equipped with a FTIR imaging analytical system to measure the concentration of different gases that were produced during the NH_3 based SCR of NO. The PSR and SSR system and the modifications of SSR system are described in detail in this chapter. Synthesis method of the catalysts used in the PSR and SSR studies is also described in this chapter. Finally, a brief description of the catalyst characterization technique is provided. X-ray diffraction and atomic absorption spectroscopy were performed to understand the quality of the catalysts tested in the PSR.

2.2. High-throughput reactor

Extensive research has been performed in the last decades toward the development of HTR with parallel analysis techniques to study heterogeneous catalysts [19, 79–81]. HTR is the best choice in the discovery of new catalyst because of its ability to screen multiple catalysts in a short period of time and at the same condition. In this section the PSR and the SSR are discussed in detail.

2.2.1. Primary screening reactor

The picture and scheme of PSR is shown in Figure 2.1. The reaction gas mixture enters from the top of the reactor and goes to each one of the 16 channels. Multiple mass flow controllers (Brooks® Model 5850E) allow a wide range of feed gas concentrations, compositions, and flow rates to be explored. The channels are vertical with ID 0.38in and height 0.24in. Quartz wool and quartz filter papers (VWR Catalog Number 28150-897) were used at the bottom of the channels to hold the catalyst. A quartz filter paper (VWR Catalog Number 21431-422) placed on top of 16 channels ensured plug flow through the catalysts. Two copper gaskets (Duniway Stockroom Corp., Part No. G-450 and G-275) placed in between the reactor plates prevented leakage of the gas from the reactor. A temperature controller (Omega Engineering, Part No. CSC32K) along with a high temperature heat tape (Omega Engineering, Part No. DHT051060LD) were used to heat the reactor to the required temperature. The reactor was wrapped with insulation and aluminum foil to prevent significant heat loss. The reactor has 16 outlets which are connected with the gas phase array (GPA). The outlets are stainless steel tubing with OD 1/16in (McMaster-Carr Catalog Number 51755K37).
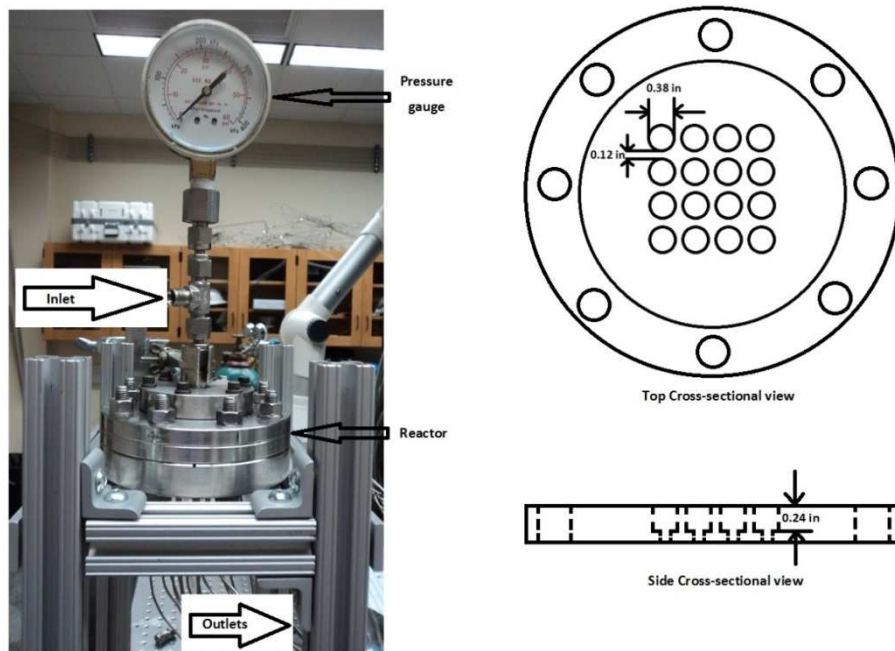
Figure-2.1: Primary screening reactor system

2.2.2. Secondary screening reactor

The SSR system consists of 16 parallel reactors, mass flow controllers, H_2O injection system, temperature controller, heat-traced tubing and FTIR imaging system as shown in Figure-2.2 [11, 73-77]. The reaction gas mixture passes through an evaporative mixer and enters the reactor system from top, where the gas mixture is separated into sixteen individual streams, going to each one of the 16 reactors. Multiple mass flow controllers (Brooks® Model 5850E) allow a wide range of feed gas concentrations, compositions, and flow rates to be explored. After reaction, the product gases pass through the GPA and analyzed in parallel by FTIR imaging system.
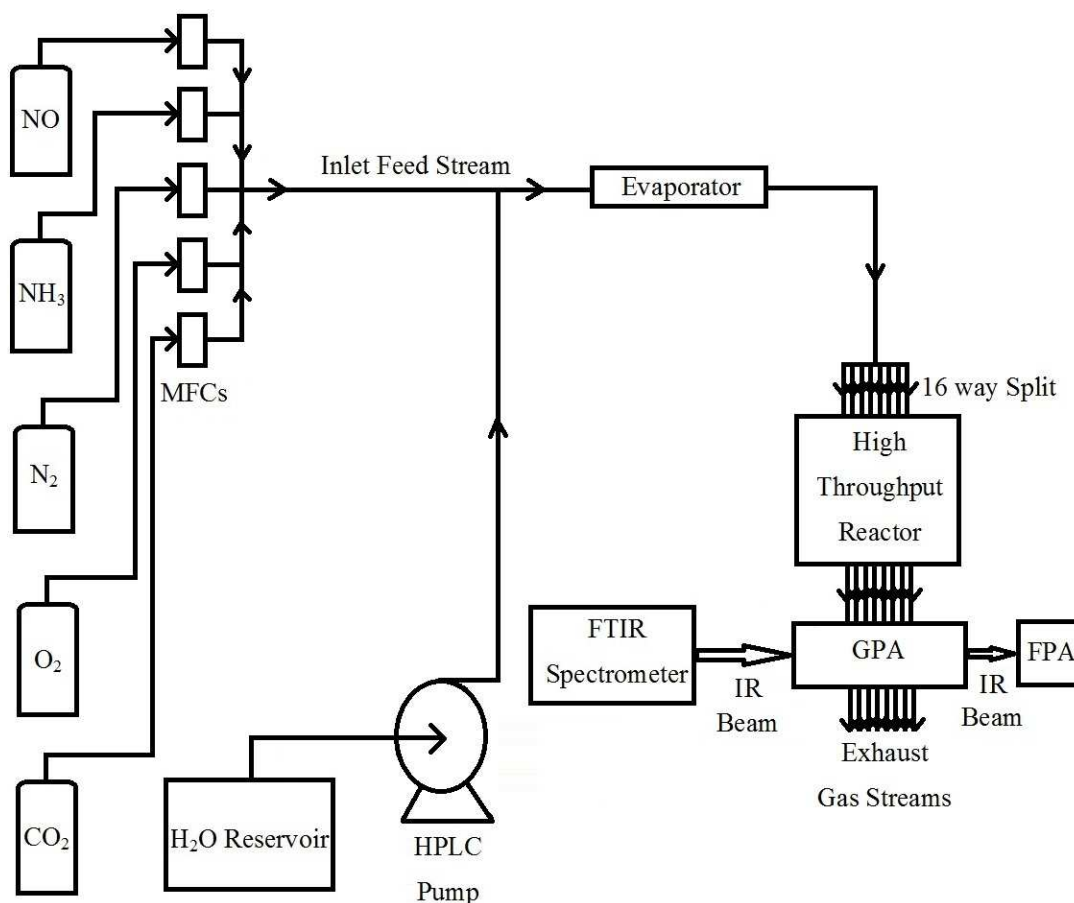
Figure-2.2: Schematic of Secondary screening reactor system.

After splitting, the feed gas flows through 1/16in stainless steel capillaries with 0.007in ID (Sigma-Aldrich, stock number 56717) before passing through the reactor tubes. Capillary tubes ensure approximately equal amount of flow through each reactor tube. For a typical experiment without H_2O injection at 120^oC using 1800sccm total flow rate through the reactor channels with heat traced lines, the capillaries provided $\approx$ 68psig pressure drop. The pressure drop yielded near-atmospheric pressure conditions at the catalyst bed. The pressure drop increases with the increase of temperature and H_2O

21

injection. To decrease the pressure drop, 1/16in stainless steel capillaries with 0.01in ID (Sigma-Aldrich, stock number 56723) has recently been installed in place of the old capillaries. For a typical experiment without H_2O injection at 120^oC using 1800sccm total flow rate through the reactor channels with heat traced lines, the capillaries provided $\approx$ 22psig pressure drop. Figure-2.3 shows a photograph of the SSR.
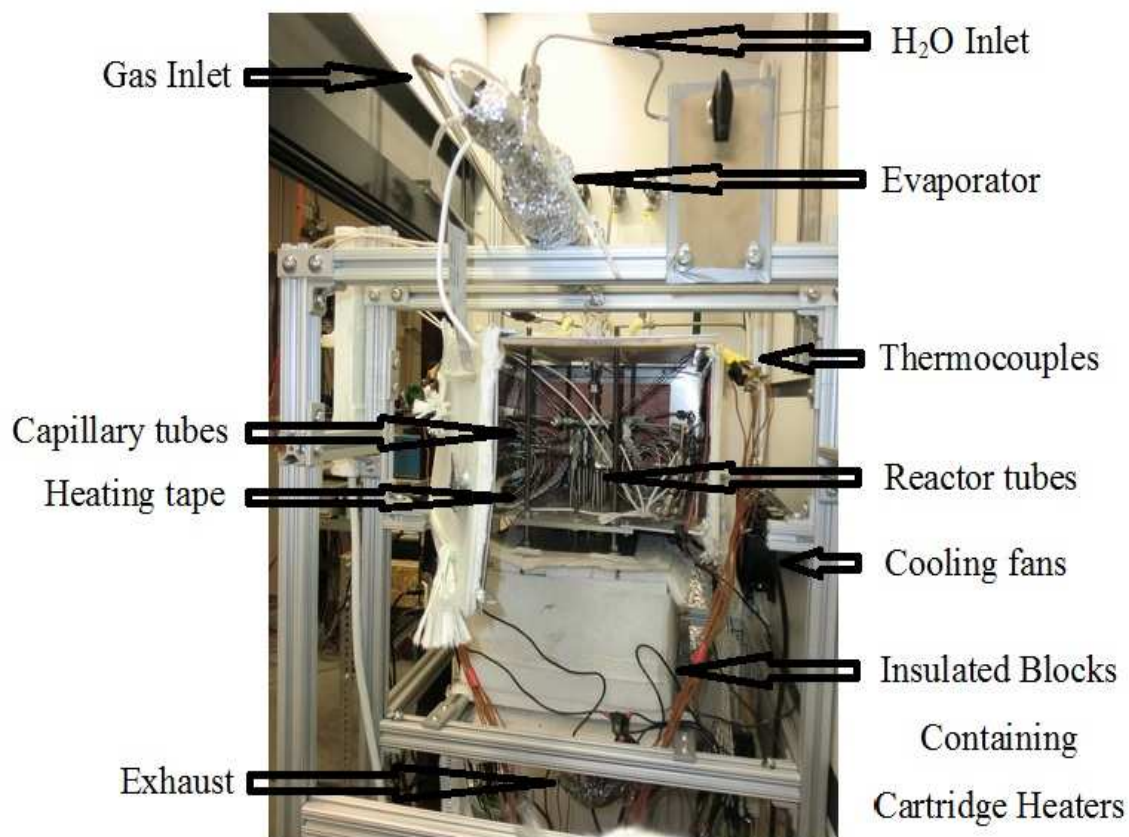
Figure-2.3: A photograph of the Secondary screening reactor.

The reactors are removable 316 grade stainless steel tubes with ¼ in OD, 0.18in ID and 5.5in length. The reactors are typically loaded with powder catalyst samples of 150mg. To hold the catalysts in the vertically-aligned tubes, the bottom of each tube is fitted with a stainless steel porous disc with pore size of 10μm (Chand Eisenmann

22

Metallurgical, part no. 102096). The discs are hammered into the bottom of tubes using a mallet so that the bottom of each disc is level with the edge of the reactor tube prior to loading the catalysts. Two hollow hexagonal blocks (3.5in length and ¾in width) compressed with o-rings (McMaster-Carr, Catalog Number 6540K165) hold each reactor tubes inside the reactor. The o-rings are used to prevent leakage of the inlet streams of the reactors. Double-Seal Viton® Fluoroelastomer o-rings were chosen for good acid resistance, fair alkali resistance and high temperature resistance. The reactors were heated using 16 cartridge heaters (Watlow, Part No. G3A121-L18H) placed in the hexagonal blocks inside the bottom part of the reactor. A schematic of configuration of reactor tubes and cartridge heaters is shown in Figure-2.4. In Figure-2.4, all 16 reactor channels are labeled individually from 0 to 15. Reactors marked with "X" are unused because the system can handle only 16 reactors. The dashed marking border shows the position of ceramic block insulation.
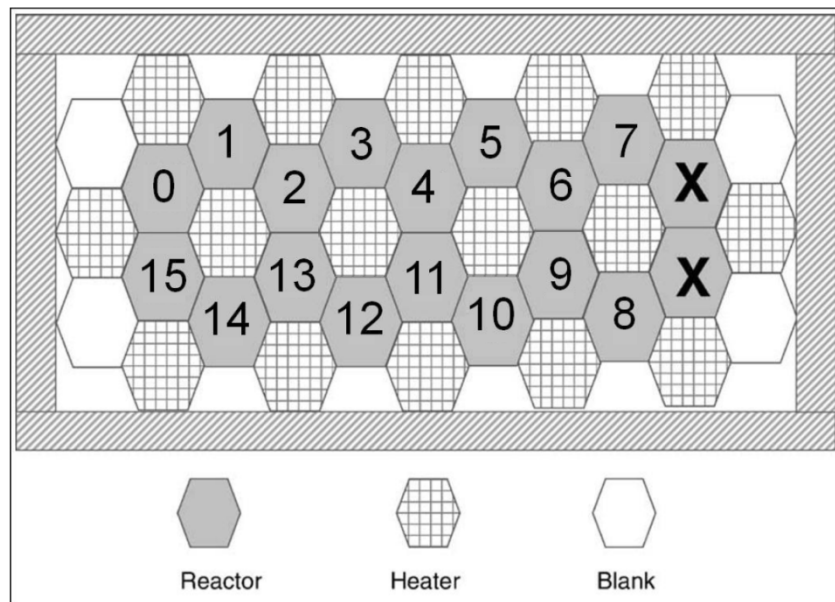
Figure-2.4: Top view of location of reactor tube and cartridge heater.

Each reactor tube is fitted with K-type thermocouple (Omega Engineering, Part No. KMQ316SS-032U-18) placed in the catalyst bed just above the porous disc for individual reactor temperature monitoring. The thermocouples were inserted from top of each tube through 15% graphite / 85% Vespel® ferrules (SGE Chromatography Products) and capped to the tube using ¼in nuts. Reactor tube 12 is fitted with an additional thermocouple to provide the temperature feedback for the temperature controller (Omega Engineering, Part No. CN77332-C2). This thermocouple is placed slightly above the catalyst bed to minimize the effect of any exothermic or endothermic catalytic reactions on the temperature controller. LabVIEW program (LabVIEW^{TM} 2001 Service Pack 1, National Instruments, Austin, TX, USA) is used to monitor the temperature for each reactor. A screenshot of this program is shown in Figure-2.5. The response of each of the sixteen thermocouples is shown in the left side, as well as plotted in real-time at the center of the screen. As shown in Figure-2.5, for a set point of 450°C, temperature of reactor 0 and 15 deviate by as high as ~ 8%.
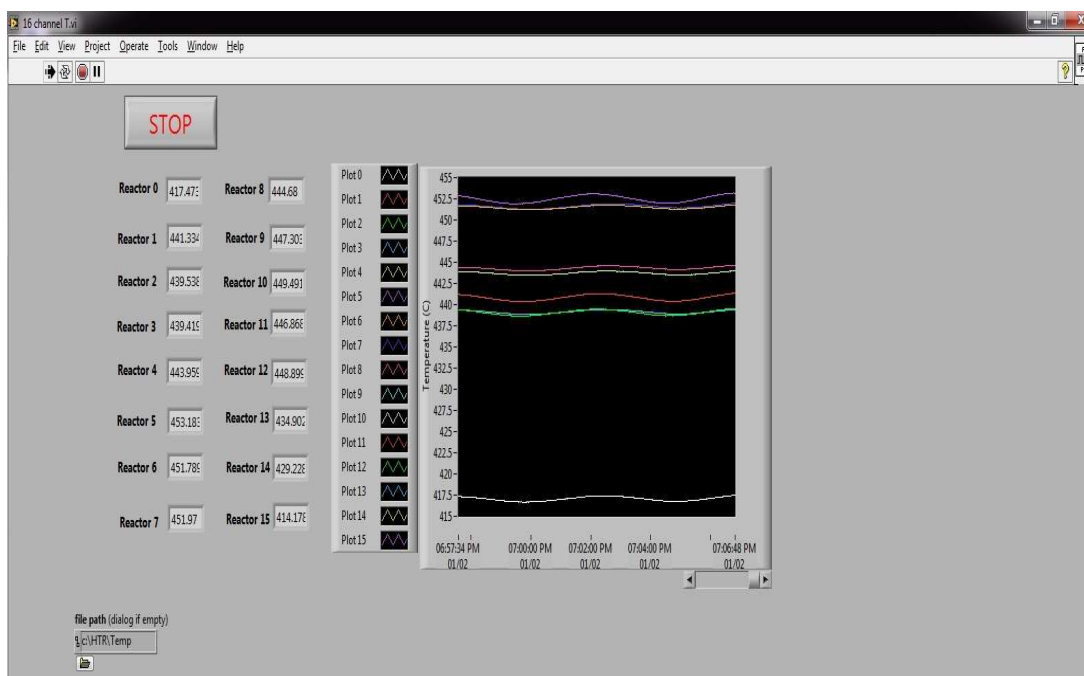
Figure-2.5: LabVIEW program for monitoring the temperature of individual reactor channel.

The reactors can be operated in a temperature range between room temperature and approximately 780°C and WHSV of 0.75L/min-gm (Gas hourly space velocity of ~ $10300hr^{-1}$). A high-performance liquid chromatography (HPLC) pump (Hitachi, L-2130) was used for H_2O injection at a rate of 0.072 ml/min into the evaporative mixer. The mixer is a 316 grade stainless steel tube of 1in OD, 0.93in ID and 1ft length (McMaster-Carr, Catalog Number 5240T15). The mixer is filled with stainless steel washers to increase the internal evaporative surface area. The mixer is wrapped with a heating tape (Omega Engineering, Part No. FGH051-080) to heat the mixer to a temperature in excess of the boiling point ($\approx 250^{\circ}$C) of H_2O at elevated pressure. The carrier gas passes through the mixer to combine with steam and the combined gas feed continues through heat-traced lines to the reactor inlet. The entire set-up was completely heat-traced to avoid condensation of H_2O after the mixer and the reactor inlet. Since the exhaust gas contains

more than 5% steam and the boiling point of that gas mixture is more than $40^{o}C$ all exhaust lines were also heated to around $60\text{-}70^{o}C$ to prevent the condensation of H_2O inside the exhaust streams and increase of pressure drop.

2.3. Fourier transform infrared imaging analysis

FTIR imaging is the main analytical technique used in these high throughput studies [11, 73-77]. The FTIR spectrometer (Bruker Equinox 55) is used as an infrared (IR) light source, GPA is used as sample gas holder and Focal Plane Array (FPA) detector is used as an IR detecting element. Figure-2.6 shows the optical layout for the FTIR imaging set-up. During the experiment an IR beam exits through the right port of FTIR spectrometer and is reflected by a gold plated mirror to a zinc selenide (ZnSe) meniscus lens that spreads the beam. The beam is then collimated by a barium fluoride (BaF_2) lens and is directed through the GPA, where IR-active molecules of the 16 reactor effluents partially absorb IR light. Upon exiting the GPA, the IR light is focused by another BaF_2 lens and is collimated by another ZnSe lens. The beam then impinges upon a FPA detector. All optical elements are placed inside two houses made of polycarbonate sheets. The houses are continuously purged with CO_2 free air from a purge gas generator (Parker-Balston, Model No. 75-62) to maintain a constant, reduced background signal from atmospheric CO_2 and water vapor.
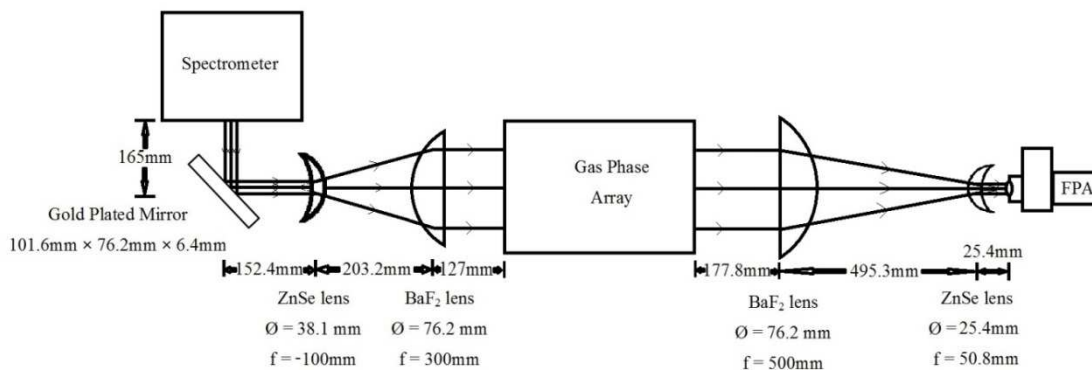
Figure-2.6: Optics configuration for FTIR imaging. Lens type, diameter (Ø), and focal length (f) are shown.

The FTIR spectrometer (Bruker Equinox 55) is operated using OPUS (Version 4.0 Build: 4, 0, 24, Bruker Optics Inc., Billerica, MA, USA). In OPUS data are collected between 4000 and 400 cm^{-1} with a resolution of 8 cm^{-1}. The mirror velocity is adjusted to 2850 Hz. Double sided, fast return acquisition mode is chosen to get a centered interferogram.

2.3.1. Gas Phase Array

A GPA sampling cell is used to analyze the effluent streams from all 16 channels of the HTR simultaneously [11, 20, 53, 69, 77]. The GPA is composed of 16 tightly packed stainless steel tubes, each with a separate gas inlet and outlet, and capped at each end with IR transparent windows as shown in Figure-2.7. Each stainless steel tube is 30cm in length with OD 3/8in (ID 0.305in). 1/8in OD tubes were welded to the walls of the each channel as inlet and outlet. Both ends of the GPA were capped by ZnSe windows (ISP Optics, part no. AR312-ZC-W-50-3) of 50.8mm in diameter with a 3μm anti-reflective coating, which are transparent over a large spectral range and are inert to most reaction gases. Double-Seal Viton® Fluoroelastomer o-rings were used between the

ends of the channels and windows to make a good seal. The inlets and outlets to each channel of the GPA are near the windows to minimize the dead volume. The GPA was wrapped with heating tape and aluminum foil and heated to around $70^{\circ}C$ to prevent the condensation of H_2O. The IR light is transmitted through all tubes simultaneously allowing the products from each channel of the reactor to be analyzed in parallel.
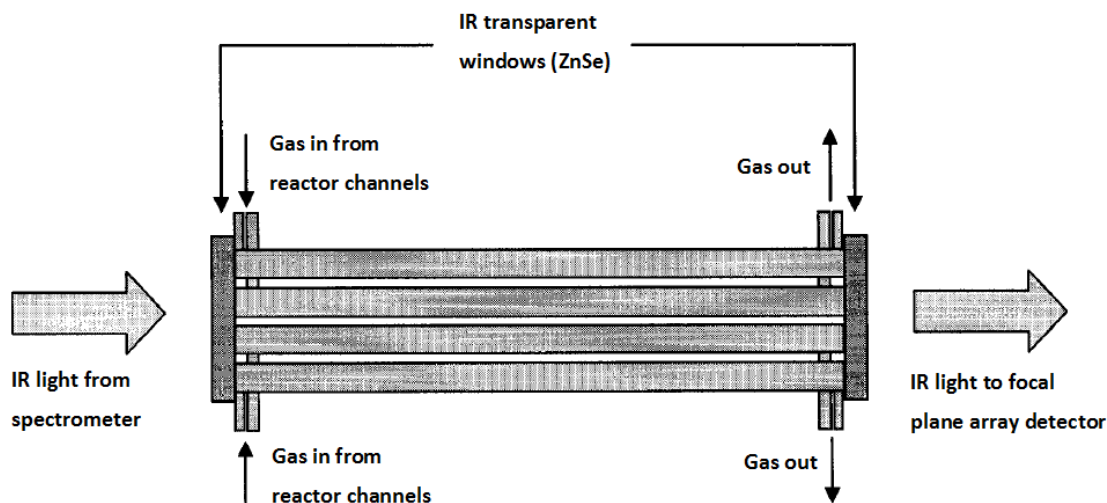
Figure-2.7: Gas Phase Array (GPA) [69].

2.3.2. Focal Plane Array Detector

A Liquid Nitrogen Dewar (Santa Barbara Focalplane, SBF161) with mercury-cadmium-telluride (MCT) detector consisting of a 128×128 grid of pixels is used as the FPA detector. The FPA is used to generate a full spectral image. Each pixel of the FPA is an independent IR detector capable of collecting a full interferogram. The FPA detector has a viewing window of diameter 25.15mm, thickness 1.1mm and is operated at a frame rate of 1610 Hz using WinIR (Version 3.7.3.0, Santa Barbara Focalplane, Goleta,

CA, USA). The FPA can detect 16384 pixels and record 32 interferograms in approximately one minute.

2.3.3. Quantitative IR Analysis

IR spectra of different gases were analyzed using JAIMP (Just Another Image Manipulation Program) designed in-house and GRAMS (Version 9.1, Thermo Fischer Scientific Inc., Waltham, MA, USA) softwares. A calibration file is generated to determine the unknown concentration of a gas in a mixture.

JAIMP is good for calibration if the IR peaks of the gases under analysis are not overlapping, i.e. univariate calibration. The IR spectrum of CO_2 shown in Figure-2.8 has three distinct types of vibrational modes: bending, asymmetric stretching and combination bands. Bending mode is outside the detection range of ZnSe windows and combination bands overlap with the stretching vibration modes of water. However, the asymmetric stretching vibration mode peak of CO_2 does not overlap with any other IR active species. Hence, a univariate calibration was developed in JAIMP and GRAMS to predict the unknown concentration of CO_2.
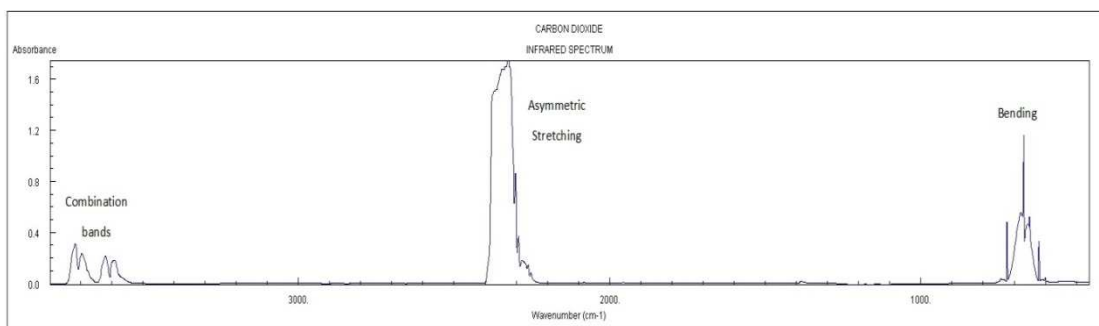
Figure-2.8: IR spectrum of CO_2 (Reproduced from NIST Webbook).

Univariate calibration follows the Beer's law which states that, the measured absorbance value for a given spectral band of species of interest is linearly related to both the concentration of the species in the sample and the path length of the IR light through the sample. Beer's law is only valid for absorbance values < 0.1 (or low concentrations). For higher concentrations, a non- linear term is added to the Beer's law to improve the calibration efficiency as shown in equation (2.1).

$$C = x_1 A^2 + x_2 A \dots (2.1)$$

where, C is the unknown concentration, A is the measured absorbance and x_1 and x_2 are fitting parameters incorporating both path length and absorptivity.

Calibration curve was generated by passing different concentrations of a gas through the GPA and calculating the corresponding peak area in JAIMP. The calibration curve can be a linear line or a second degree polynomial based on the intensity (Height) of the peak. If the peak intensity is more than 0.5 the calibration curve is likely to be a second degree polynomial, rather than a straight line. Figure-2.9 shows a calibration of CO_2 using JAIMP. This calibration was then used to determine the unknown concentration of CO_2 in a gas mixture.
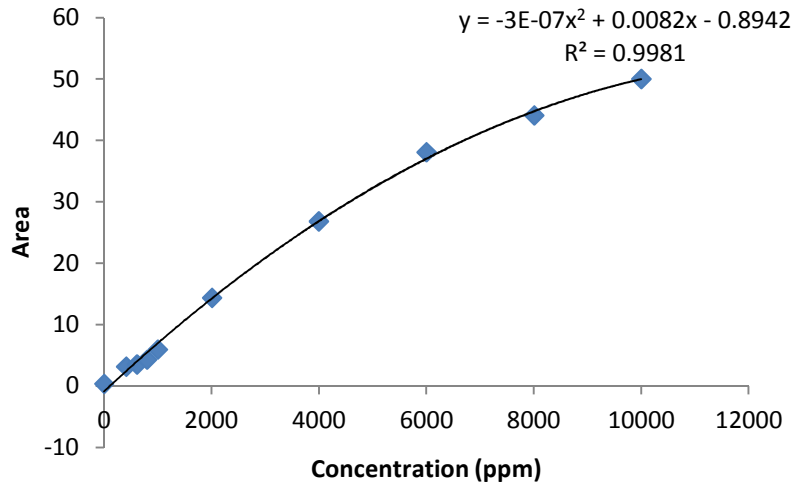
Figure-2.9: Calibration of CO_2

GRAMS is useful for the implementation of both univariate and multivariate calibration. The main advantage of GRAMS over JAIMP is the scope of the multivariate calibration. Multivariate calibration allows any number of components to be analyzed and extend the quantitative usefulness of IR analysis to complex mixtures. GRAMS utilizes the factor-based methods of principal component regression (PCR) and partial least squares 1 and 2 (PLS-1 and PLS-2) for univariate and multivariate calibration study. The basic principle of these methods is that, the entire IR spectrum can be utilized to quantify concentrations instead of a single spectral frequency.

PCR method combines the Principal Component Analysis (PCA) spectral decomposition with an Inverse Least Squares (ILS) regression method to create a quantitative model for complex samples. It is a two-step process consists of the PCA eigenvectors (factors) and scores (scaling coefficients) calculation and then regression of the scores against the constituent concentrations. An extension of PCR is done for PLS-1 and PLS-2 where the decomposition on both the spectral and concentration data is

31

performed simultaneously. The factors and scores are matched iteratively until the desired number of factors is calculated. The difference between PLS-1 and PLS-2 is that PLS-2 calibrates for all constituents simultaneously, whereas in PLS-1, a separate set of scores and eigenvectors is calculated for each constituent of interest. Therefore, PLS-1 should give more accurate predictions than PCR or PLS-2. Details on all these methods and their relative advantages and disadvantages have been discussed in great depth in references [82-83].

In GRAMS, total number of factors used to fit the training data set plays a very important role. As the number of factors to model the training data set increases the eigenvectors begins to model the system noise which usually provides the smallest contribution to the data. Calibration models that include noise vectors or more vectors than are actually necessary to predict the constituent concentrations are called overfit, whereas models that do not have enough factors in them are known as underfit. The optimum number of factors is normally decided by calculating the PRESS (Prediction Residual Error Sum of Squares) for every possible factor. PRESS is calculated by building a calibration model with a number of factors, then predicting some samples of known concentration (usually the training set data itself) against the model. The sum of the squared difference between the predicted and known concentrations gives the PRESS value for that model. The smaller the PRESS value, the better the model is able to predict the concentrations of the calibrated constituents.

Calibration curve is generated in GRAMS by analyzing a number of spectra (≥ 5) of different concentrations of a gas and predicting the corresponding concentration based on the peak area. The calibration curve is a linear line as shown in Figure-2.10. Figure-

2.10 shows the univariate calibration of CO_2 developed by PCR method. This calibration was then used to predict the unknown concentration of CO_2 in a gas mixture.
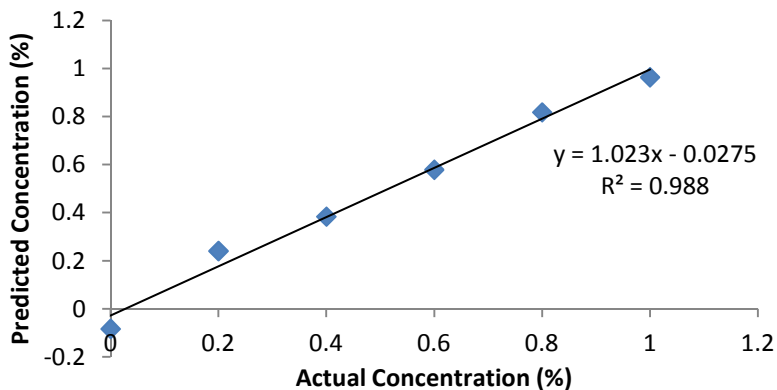
Figure-2.10: Calibration of CO_2 developed by PCR method.

To analyze the overlapping IR spectra of NO and H_2O as shown in Figure-2.11, multivariate calibration was developed in GRAMS. The most important step in the development of a multivariate calibration is the careful design of the calibration experiments.
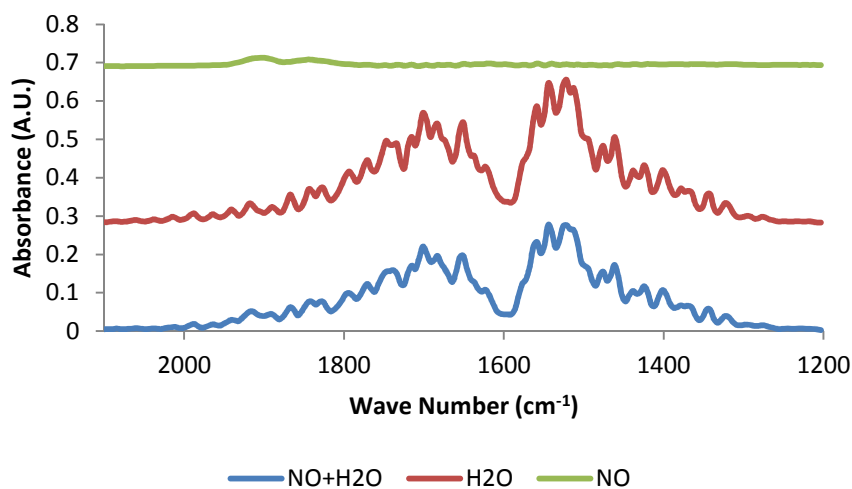
Figure-2.11: Spectra showing overlapping IR bands of NO and H_2O.

The calibration data set must be designed to span the entire expected concentration range and the variables of interest should be varied independently so that all possible interferences in the measured signal are present during the calibration. For our case, the concentration of NO was varied over 0 to 1500ppm and that of H_2O over 0 to 5.5% as shown in Figure-2.12. Once the training data were collected and a multivariate calibration was developed, independent samples were analyzed with the model to validate the calibration model.
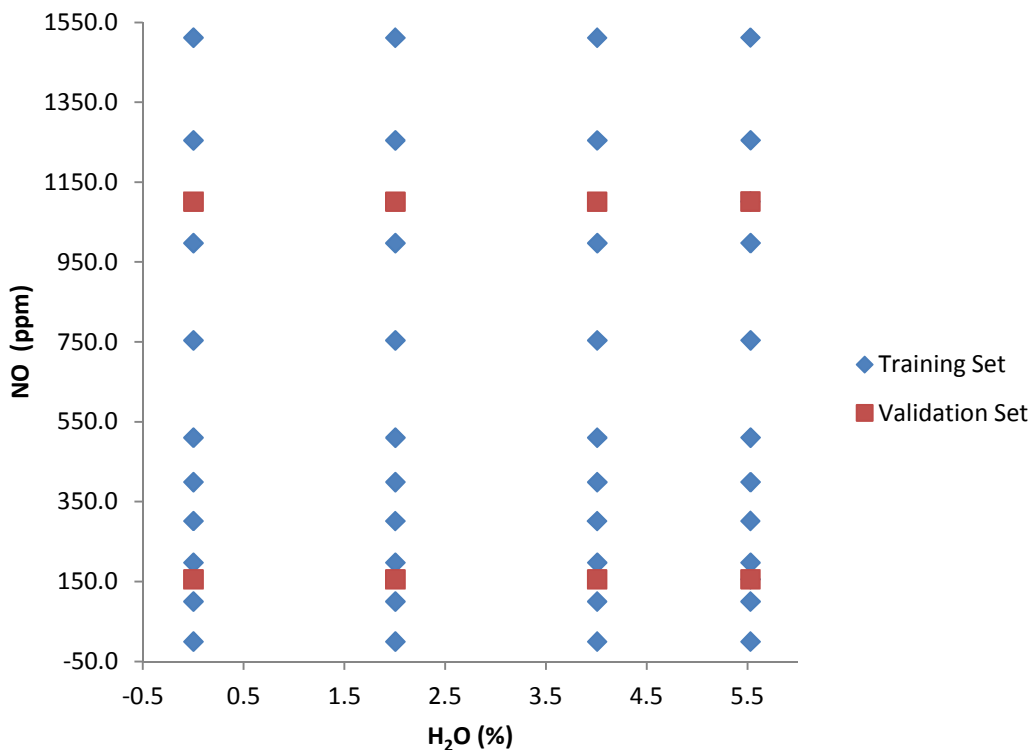
Figure-2.12: Multivariate Calibration of NO and H_2O.

2.4. Catalyst preparation for primary screening reactor study

All catalysts used in PSR study were synthesized using the incipient wetness impregnation technique which is extensively used in laboratory scale for the preparation

of heterogeneous catalysts [84]. Aluminum oxide gamma-phase, 99.97% (metals basis, 3micron APS Powder, S.A. 80-120m^2/g, source: Alfa Aesar, product no. 39812) and Titanium(IV) oxide (nanopowder, ~21 nm particle size, ≥99.5% trace metals basis, source: Sigma Aldrich, stock no. 718467) were used as supports. Silver nitrate, ACS, 99.9+% (metals basis, source: Alfa Aesar, product no. 11414), Tetraammineplatinum(II) chloride monohydrate (source: Alfa Aesar, product no. 10544), Cobalt(II) nitrate hexahydrate, ACS, 98.0-102.0% (source: Alfa Aesar, product no. 36418), Tetraamminepalladium(II) chloride monohydrate, 99.9% (metals basis), Pd 39% min (source: Alfa Aesar, product no. 11036), Copper(II) nitrate hemi(pentahydrate), ACS, 98.0-102.0% (source: Alfa Aesar, product no. 12523) and Rhodium(III) chloride hydrate, Rh 38.5-45.5% (source: Alfa Aesar, product no. 11032) were used as Ag, Pt, cobalt (Co), Pd, Cu and Rh precursors, respectively. Synthesis of 1% Pd/γ-Al$_2$O$_3$ using incipient wetness impregnation technique is described below as an example. The naming convention for each catalyst is based on the nominal weight loading e.g. 1% Pd/γ-Al$_2$O$_3$ means 1% (wt) Pd is supported on γ-Al$_2$O$_3$. At first 0.0496gm of Pd precursor was dissolved in 5ml of deionized water (DI H$_2$O). Then, 1.98gm of γ-Al$_2$O$_3$ was added to the solution and the solution was heated at 80-90°C to evaporate the H$_2$O while keeping the solution under stirring. After drying of H$_2$O, precursor was left on the surface of γ-Al$_2$O$_3$. The impregnated support was then taken in another beaker and dried in an oven at 120°C for 24hours to remove H$_2$O completely. At last, the catalysts were calcined at 550°C for 3h @ 5°C/min.

2.5. Catalyst preparation for secondary screening reactor study

All catalysts used in SSR study were synthesized using the ion exchange technique which is another extensively used technique in laboratory scale for the preparation of heterogeneous catalysts [84]. Zeolite beta, ammonium (S.A. 680m^2/g, SiO$_2$:Al$_2$O$_3$ = 25:1, source: Alfa Aesar, product no. 45873), Zeolite ZSM-5, ammonium (S.A. 425m^2/g, SiO$_2$:Al$_2$O$_3$ = 23:1, source: Alfa Aesar, product no. 45879), Zeolite ZSM-5, ammonium (S.A. 400m^2/g, SiO$_2$:Al$_2$O$_3$ = 30:1, source: Alfa Aesar, product no. 45880), Zeolite ZSM-5, ammonium (S.A. 425m^2/g, SiO$_2$:Al$_2$O$_3$ = 80:1, source: Alfa Aesar, product no. 45882), Zeolite ZSM-5, ammonium (S.A. 400m^2/g, SiO$_2$:Al$_2$O$_3$ = 200-400:1, source: Alfa Aesar, product no. 45883) and Zeolite SSZ-13, ammonium synthesized at home were used as supports. Copper(II) nitrate hemi(pentahydrate), ACS, 98.0-102.0% (source: Alfa Aesar, product no. 12523), Iron(III) nitrate nonahydrate, ACS, 98+% (metals basis, source: Alfa Aesar, product no. 12226), Manganese(II) nitrate hydrate, 99.98% (metals basis, source: Alfa Aesar, product no. 87848), Cobalt(II) nitrate hexahydrate, ACS, 98.0-102.0% (source: Alfa Aesar, product no. 36418), Nickel(II) nitrate hexahydrate, 98% (source: Alfa Aesar, product no. A15540), Zinc nitrate hexahydrate, 99% (metals basis, source: Alfa Aesar, product no. 12313), Silver nitrate, ACS, 99.9+% (metals basis, source: Alfa Aesar, product no. 11414), Indium(III) nitrate hydrate, In 29% min (source: Alfa Aesar, product no. A18252), Barium nitrate, ACS, 99+% (source: Alfa Aesar, product no. 12194), Lanthanum(III) nitrate hexahydrate, 99.9% (REO, source: Alfa Aesar, product no. 12915), Cerium(III) nitrate hexahydrate, REacton®, 99.5% (REO, source: Alfa Aesar, product no. 11329), Neodymium(III) nitrate hydrate, 99.9% (REO, source: Alfa Aesar, product no. 12912), Gadolinium(III) nitrate

hydrate, 99.9% (REO, source: Alfa Aesar, product no. 12917) and Tin(II) chloride dihydrate, 98% (source: Alfa Aesar, product no. A14610) were used as Cu, Fe, Mn, Co, Ni, Zn, Ag, In, Ba, La, Ce, Nd, Gd and Sn precursors, respectively. Synthesis of Zeolite SSZ-13, ammonium and preparation of Cu-Zeolite-beta by ion exchange technique are described below as an example.

2.5.1. Synthesis of SSZ-13, ammonium

At first 74gm Adamantium hydroxide, 25% (source: SACHEM Inc. part code 2825) and 36.59gm Tetraethoxysilane, 99.9% (source: Alfa Aesar, product no. 40251) were mixed in a beaker. The solution was stirred for an hour. Then 7.5 ml of DI H_2O was added to the solution while keeping the solution under stirring. After 30min 2gm Aluminum ethoxide (source: Alfa Aesar, product no. 41336) was added to the solution and the solution was stirred for 5hr to obtain a homogeneous solution. The solution was then transferred to Teflon-lined autoclaves and heated at 140^oC for 6 days in an oven. The products are recovered by centrifuging the solution at 15^oC @ 8000RCF for 20min. The products are then dried at 70^oC for 2hr. At last the products were calcined at 550^oC for 8hr @ 5^oC/min to obtain Zeolite SSZ-13.

Zeolite SSZ-13, ammonium was obtained by ammonium ion exchange to Zeolite SSZ-13. At first 4gm of Ammonium nitrate, ACS, 95% min (source: Alfa Aesar, product no. 12363) was dissolved in 500ml of DI H_2O. Then, ~ 8gm of Zeolite SSZ-13 was added to the solution and the solution was heated at ~ 80^oC in an oil bath for 22hr while keeping the solution under stirring. The solution was cooled and vacuum filtered to obtain ammonium ion exchanged Zeolite SSZ-13. The obtained zeolite was washed by DI H_2O

to remove residual ammonium precursor and dried in an oven at 70°C for 2hr to remove H$_2$O completely.

2.5.2. Catalyst preparation by ion exchange technique

At first 1.163gm of Cu precursor was dissolved in 100ml of DI H$_2$O. Then, 1.5gm of Zeolite beta, ammonium was added to the solution and the solution was heated at ~ 80°C in an oil bath for 2hr while keeping the solution under stirring. The solution was cooled and vacuum filtered to obtain Cu ion exchanged zeolite beta. The obtained zeolite was washed by DI H$_2$O to remove residual Cu precursor and dried in an oven at 120°C for 2hr to remove H$_2$O completely. At last, the catalysts were calcined at 500°C for 2hr @ 2°C/min.

2.6. Reaction conditions

Two different reactions were carried out in PSR and SSR. CO oxidation was used as a benchmark reaction to validate the effectiveness of the PSR, while the SSR was used to study NH$_3$ based SCR of NO.

2.6.1. Carbon monoxide oxidation using primary screening reactor

The PSR was tested using the CO oxidation reaction. For CO oxidation reaction a diverse library of catalysts were used. This library consisted of calcined TiO$_2$, calcined γ-Al$_2$O$_3$, 1% Pt/γ-Al$_2$O$_3$, 1% Rh/γ-Al$_2$O$_3$, 1% Pt/TiO$_2$, 1% Pd/γ-Al$_2$O$_3$, 2% Ag/γ-Al$_2$O$_3$ and two reactor tubes without catalysts. The catalysts were pretreated using an oxidation and reduction cycle. Oxidation was carried out at 450°C by flowing 240sccm of O$_2$ and 560sccm of Argon (Ar) over the catalyst beds, while the reduction was carried out at

$300^{\circ}C$ by flowing 200sccm of hydrogen (H_2) and 600sccm of Ar over the catalysts. The reaction was studied at $160^{\circ}C$-$300^{\circ}C$ @ $20^{\circ}C$ increments by flowing 1% CO, 14% O_2 and balance Ar (a total of 800sccm) over the catalysts.

2.6.2. Ammonia based selective catalytic reduction of nitric oxide using secondary screening reactor

The SSR was studied using the NH_3 SCR of NO reaction. For NH_3 SCR of NO titania-vanadia was used as the benchmark catalyst. Four reactors were left blank to check the reactivity of empty reactor tubes during the study. The reaction was studied at $150^{\circ}C$, $250^{\circ}C$, $350^{\circ}C$ and $450^{\circ}C$ by flowing 5% CO_2, 8% O_2, 1500ppm NO, 1500ppm NH_3 and balance N_2 (a total of 1800SCCM) over the catalysts. The reaction was also studied with H_2O or steam injection at $150^{\circ}C$, $250^{\circ}C$, $350^{\circ}C$ and $450^{\circ}C$ by flowing 5% steam, 5% CO_2, 8% O_2, 1500ppm NO, 1500ppm NH_3 and balance N_2 (a total of 1800SCCM) over the catalysts. After successful validation of the SSR, NH_3 SCR of NO reaction was studied at $150^{\circ}C$, $250^{\circ}C$, $350^{\circ}C$, $400^{\circ}C$, $450^{\circ}C$ and $550^{\circ}C$ by flowing 5% steam, 5% CO_2, 8% O_2, 2000ppm NO, 2000ppm NH_3 and balance N_2 (a total of 1800SCCM) over the metal promoted zeolite catalysts.

2.7. Catalyst Characterization

Characterization of the catalysts is carried out to understand the properties of the active phases, structures, and morphologies of catalysts prepared. X-ray diffraction (XRD) and atomic absorption spectroscopy (AAS) were performed during the work to understand the quality of the catalysts tested in the PSR.

2.7.1. Atomic Absorption Spectroscopy (AAS)

AAS is a widely used technique to determine the metal content on a support. AAS is used as a validation technique of the synthesis method by ensuring that the measured loading of the metal is approximately equal to the desired loading.

AAS operates on the principle that ground state atoms absorb light at a characteristic wavelength and the amount of light absorbed at low concentration is linearly related to the concentration of the metal present in the sample [85]. The atomic absorption spectrometer used for these studies was a "Perkin Elmer Aanalyst 400" Atomic Absorption (AA) system. To determine the concentration of a metal on a support a calibration curve (Concentration vs. Absorbance) is developed at the beginning of each measurement, encompassing the concentration range where the absorbance is linearly related to concentration. This concentration range largely depends on the metal and atomic absorption spectrometer used for the study. The concentration ranges of all metals mentioned in the thesis are given in Table-2.1. For developing a calibration curve, the standard solution of the metal is diluted to three or more concentrations. An example procedure for Pt samples is described below. Standard solutions of 2, 5, 10, 15, and 25 ppm Pt were prepared by diluting the stock solution of 1 mg/ml Pt in 10% HCl (Acros Organics, Product Code: 196191000). The five standard solutions were then nebulized into an air/acetylene flame operating near 2200°C. A platinum hollow cathode lamp (VWR Catalog Number 97050-254) emitting radiation with a wavelength of 265.95nm was used as a light source. The light passed through the flame containing the atomized sample and after being partially absorbed, went through a monochromator to a photomultiplier detector.

Table-2.1: The concentration ranges of some metals where absorbance is linearly related to concentration

Metal	Concentration Range (ppm)
Pt	0-25
Pd	0-5
Rh	0-7.5
Cu	0-3
Co	0-2

A digestion method was used to leach out the metal from the support. The metal is leached out from the support by dissolving a small amount of catalyst (e.g. 25mg of 1% Pt on γ-Al_2O_3) in 4ml of Aqua regia (HNO_3:HCl = 1:3). The mixture is heated in an oven at $120^{o}C$ for 3h. Distilled H_2O was added to the mixture to prepare a 25ml solution. The solution was allowed to settle for the separation of undigested support. 1ml of solution was then taken out and 9ml of distilled H_2O was added to prepare a sample solution of desired concentration (e.g. 10ppm Pt solution). 0.5ml of Lanthanum Chloride ($LaCl_3$) solution was added to the Pt solution for stabilization of Pt in the sample. As prepared sample was tested using the atomic absorption spectrometer to determine the Pt content in the catalyst. Finally, metal content in a sample catalyst was determined using the following formula.

$$Metal\ Content\ (\%)$$

$$= \frac{Conc.from\ AAS\ (ppm) \times Initial\ dilution\ volume\ (ml) \times Dilution\ Factor}{Weight\ of\ sample\ (gm) \times 10000} \dots (2.2)$$

2.7.2. X-ray Diffraction (XRD)

XRD is the most common technique used to study the characteristics of bulk crystal structure and to determine the chemical phase composition present in the catalyst. XRD is an attractive characterization technique because of its speed, ease of use and can be used to perform semi-quantitative analyses. XRD requires only small amounts of catalyst sample and it is a nondestructive technique.

Crystals consist of parallel planes formed by repetitive arrangement of atoms in three-dimensional space. These planes are separated from one another by a distance (d), which varies according to the nature of the material. When X-rays are projected onto a crystalline material diffraction pattern is produced because their wavelength is typically the same order of magnitude (1–100Å) as the spacing between planes in the crystal. For constructive interference from successive crystallographic planes of the crystal lattice, the path difference between two beams with identical wavelength and phase must be equal to an integer (n) multiple of the wavelength (λ) of the radiation. This is known as Bragg's Law:

$$n\lambda = 2d \sin\theta \ \dots \ (2.3)$$

where, $2d \sin\theta$ is the path difference between two beams and θ is the scattering angle. By measuring the intensity of scattered waves as a function of scattering angle, a diffraction pattern is obtained. Within the crystal structure, the angles of diffraction differ for the various planes. Thus every compound or element shows its own somewhat unique diffraction pattern. Where a mixture of different phases is present, the resultant pattern is

a summation of the individual patterns. X-ray diffraction also gives some information about mean particle size (τ). According to Scherrer equation:

$$\tau = \frac{K\lambda}{\beta \cos\theta} \ \ldots \ (2.4)$$

where, K is the shape factor (generally 0.9), λ is the x-ray wavelength, β is full width half maximum (FWHM) in radians, and θ is the Bragg angle. Scherrer equation is applicable to nano-scale particles, grains not larger than about 0.1μm.

A Rigaku Miniflex II powder X-ray diffractometer was used to identify the crystal phases and crystallite sizes present on the catalyst. A Cu Kα source with 1.54Å wavelength was used. The voltage was set to 45kV and current to 40mA. Spectra were collected at 2θ values of 3° to 90° using a step size of 0.02° and 2s per step. The X-ray diffractometer was calibrated using a Si crystal to find a linear correlation between instrument line broadening and 2θ. The instrument's sensitivity and resolution were high enough to accurately characterize the crystallinity of catalysts used in this study.

CHAPTER 3

Results and Discussion of primary screening reactor study

3.1. Catalyst Characterization

Five catalysts were synthesized by incipient wetness impregnation methods to study the CO oxidation reaction. AAS and XRD were performed to understand the quality of these catalysts.

AAS was used to characterize the samples prepared for the PSR study. The AAS analysis of 1% Pt/γ-Al$_2$O$_3$ is given in Table-3.1. Four samples were used to increase the accuracy of the result. The AAS result proved that the metal content of synthesized 1% Pt/γ-Al$_2$O$_3$ is approximately 1%.

Table-3.1: The AAS analysis of 1% Pt/γ-Al$_2$O$_3$

Sample No.	Conc. (ppm)	Dilution factor	Wt. of Sample (gm)	Wt. (%)	Avg. Wt. (%)	Std.
1	8.671		0.0258	0.88		
2	9.903	1.05	0.0257	1.01	1.16	0.23
3	11.36		0.0257	1.30		
4	12.17		0.0259	1.45		

XRD was used to characterize the samples prepared for the PSR study. The XRD analysis of 2% Ag/γ-Al$_2$O$_3$ is described below as an example. PDXL 2 (Version 2.1.2.0, Rigaku Corporation, Woodlands, TX, USA) was used to verify the XRD patterns and determine the particle size. Figure-3.1 shows the diffraction patterns of 2% Ag/γ-Al$_2$O$_3$. Peaks at 19.9^o, 37.4^o, 46°, 60.8^o, 67° and 78.6^o conforms the presence of γ-Al$_2$O$_3$. Two peaks at 32° and 39.7^o represents Ag$_3$O$_4$ with average particle size 80.6Å.
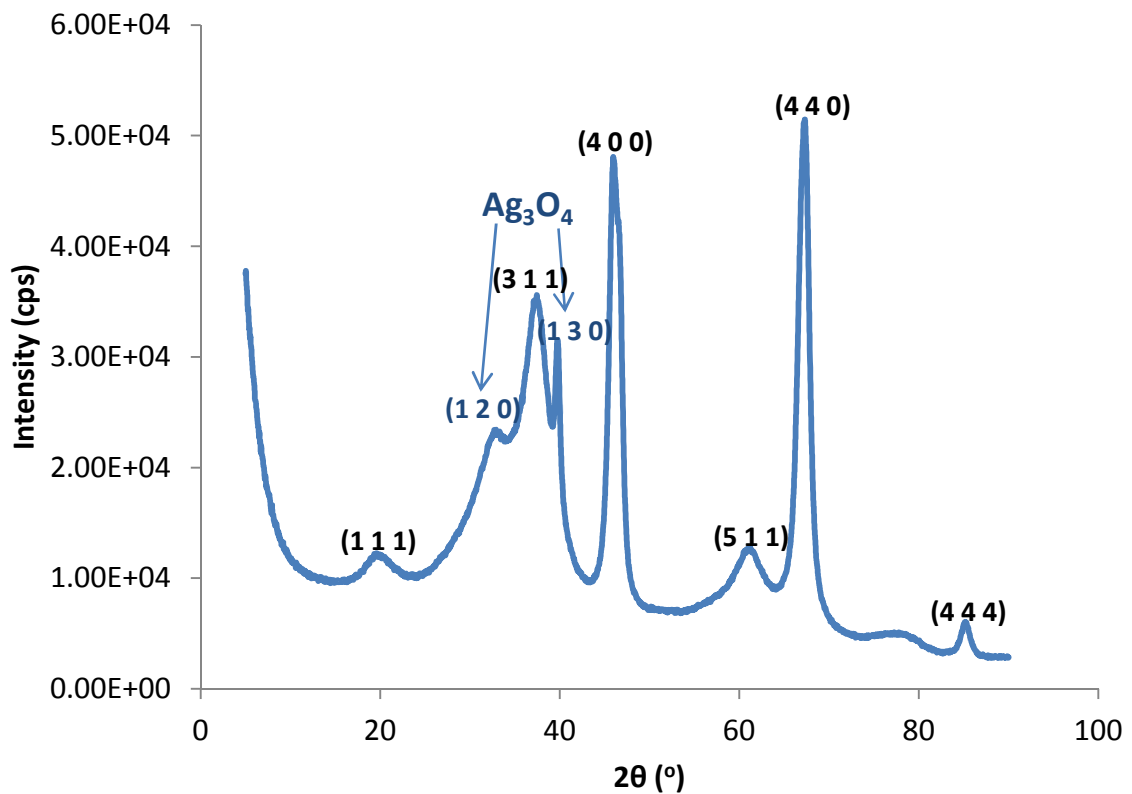

Figure-3.1: XRD Pattern of calcined 2% Ag/γ-Al$_2$O$_3$.

3.2. Validation of primary screening reactor

Results of PSR study are discussed in this section. PSR equipped with a FTIR imaging analytical system was used to test the CO oxidation. The calibration and reaction results are discussed in this section.

3.2.1. Calibration for carbon monoxide (CO) and carbon dioxide (CO_2)

The stretching vibrational mode peak of CO does not overlap with CO_2 peaks as shown in Figue-3.2. So univariate calibration was used to study the calibration of CO and CO_2. PCR, PLS-1, PLS-2 and area based JAIMP methods were used to develop the calibration of CO and CO_2.
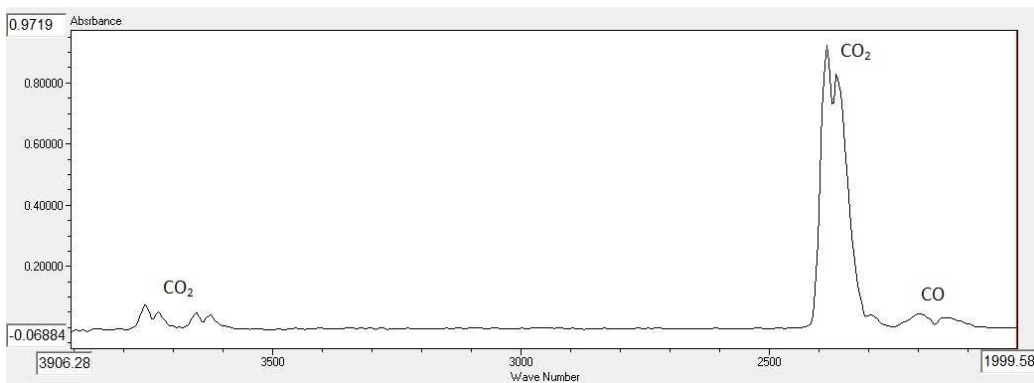
Figure-3.2: The IR spectra of CO and CO_2.

CO calibration developed by PLS-1 method is shown in Figure-3.3 as an example. The calibration curves for all 16 channels were straight lines with R^2 value ≈ 0.8.

Figure-3.3: CO calibration developed by PLS-1 method.

This calibration was validated by the prediction of a sample of known concentration as shown in Figure-3.4. 0.17% CO in Argon (Horizontal line in Figure-3.4) was used as the unknown sample to validate the calibration model. The prediction based on the calibration developed by PLS-1 method determined an average CO concentration of 0.27% with a standard deviation of 0.008%.

Figure-3.4: Validation of the CO calibration model.

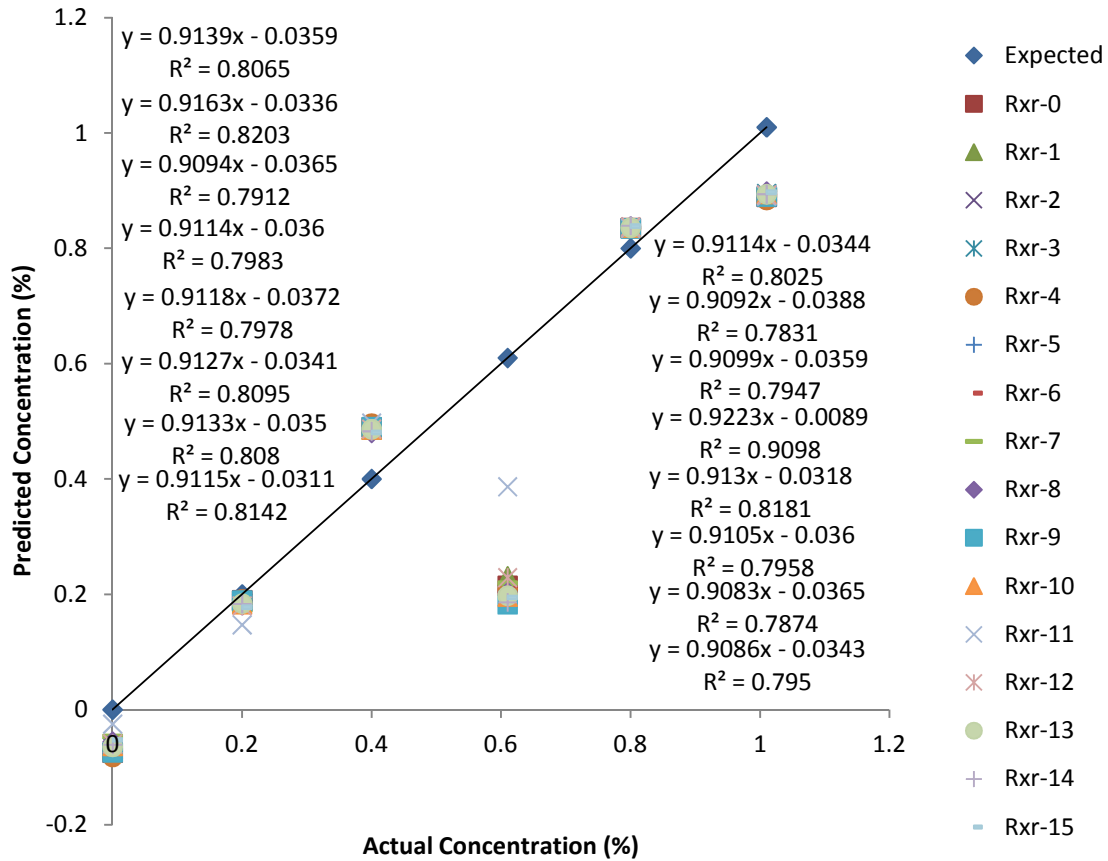CO_2 calibration developed by area based JAIMP method was second degree polynomial for all 16 channels with R^2 value $\approx$ 0.99. This calibration was validated by the prediction of a sample of known concentration as shown in Figure-3.5. 0.21% CO_2 in Argon (Horizontal line in Figure-3.5) was used as the unknown sample to validate the calibration model. The prediction based on the calibration developed by area based JAIMP method determined an average CO_2 concentration of 0.262% with a standard deviation of 0.0009%.
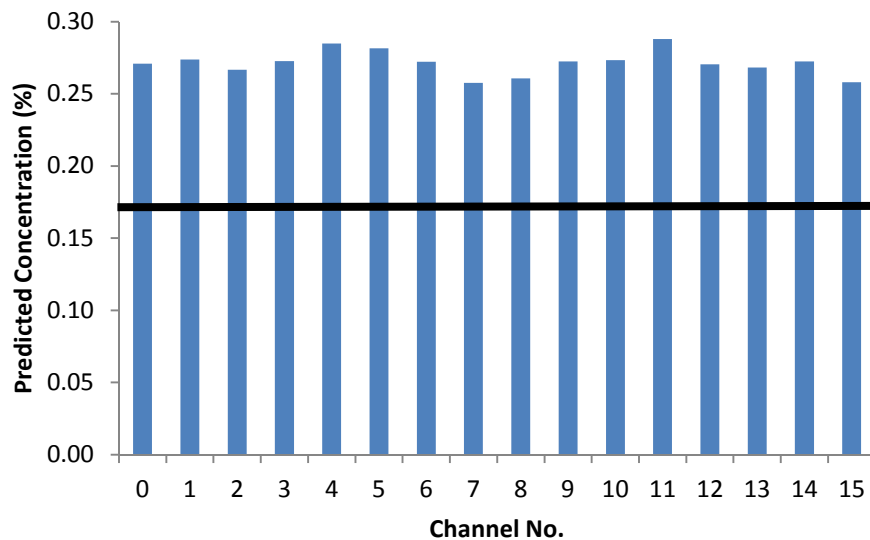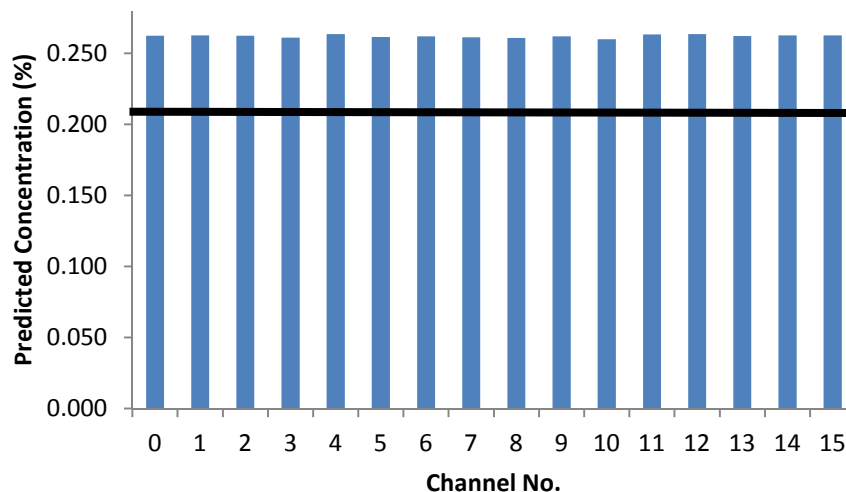
Figure-3.5: Validation of the CO$_2$ calibration model.

CO$_2$ calibration was more accurate than CO calibration and was used to predict the amount of CO$_2$ produced during the CO oxidation reaction. Over prediction was observed for both CO and CO$_2$ prediction, but the over prediction in case of CO$_2$ prediction is systematic, which can be subtracted to determine the actual concentration.

3.2.2. Carbon monoxide (CO) oxidation reaction study

CO oxidation was carried out in the PSR using a diverse library of catalysts. This library consisted of calcined TiO$_2$, calcined γ-Al$_2$O$_3$, 1% Pt/γ-Al$_2$O$_3$, 1% Rh/γ-Al$_2$O$_3$, 1% Pt/TiO$_2$, 1% Pd/γ-Al$_2$O$_3$, 2% Ag/γ-Al$_2$O$_3$. All these catalysts were loaded in two channels and two channels were left blank. The reason behind this type of loading was to check the reproducibility of result from two different channels. Figure-3.6 shows the IR spectra of channel-1 loaded with calcined TiO$_2$ during CO oxidation reaction at 200°C, as an example. The left square shaped box with 17 circles shows the relative concentration of

CO and CO_2 in real time. The color of the circle is the indicator of the relative concentration: the darker the color the higher the concentration.
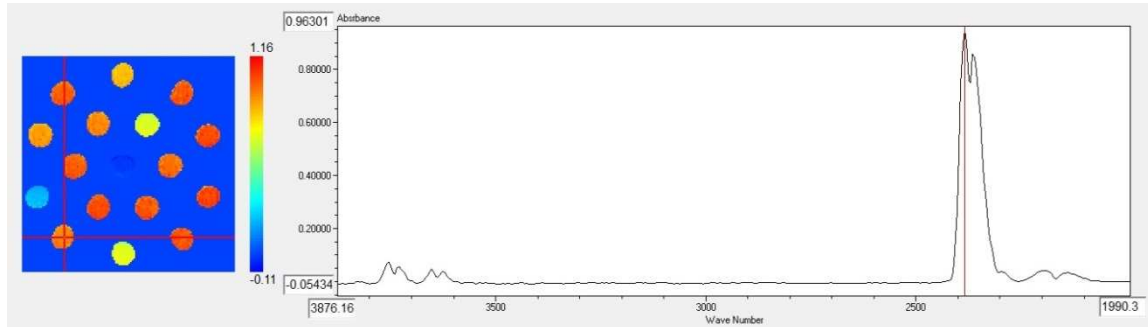
Figure-3.6: CO oxidation reaction at 200°C on calcined TiO$_2$.

The result of CO oxidation for a single run is given below in Figure-3.8. The concentration of CO_2 was measured by using the CO_2 calibration developed by area based JAIMP method. As shown in Figure-3.7, CO_2 flow rate in blank channels were higher than some channels with catalysts. This leads to a conclusion that there might be a cross talk of reaction products among the channels, since 16 channels were in close proximity with a distance of 0.12in between two neighboring channels.
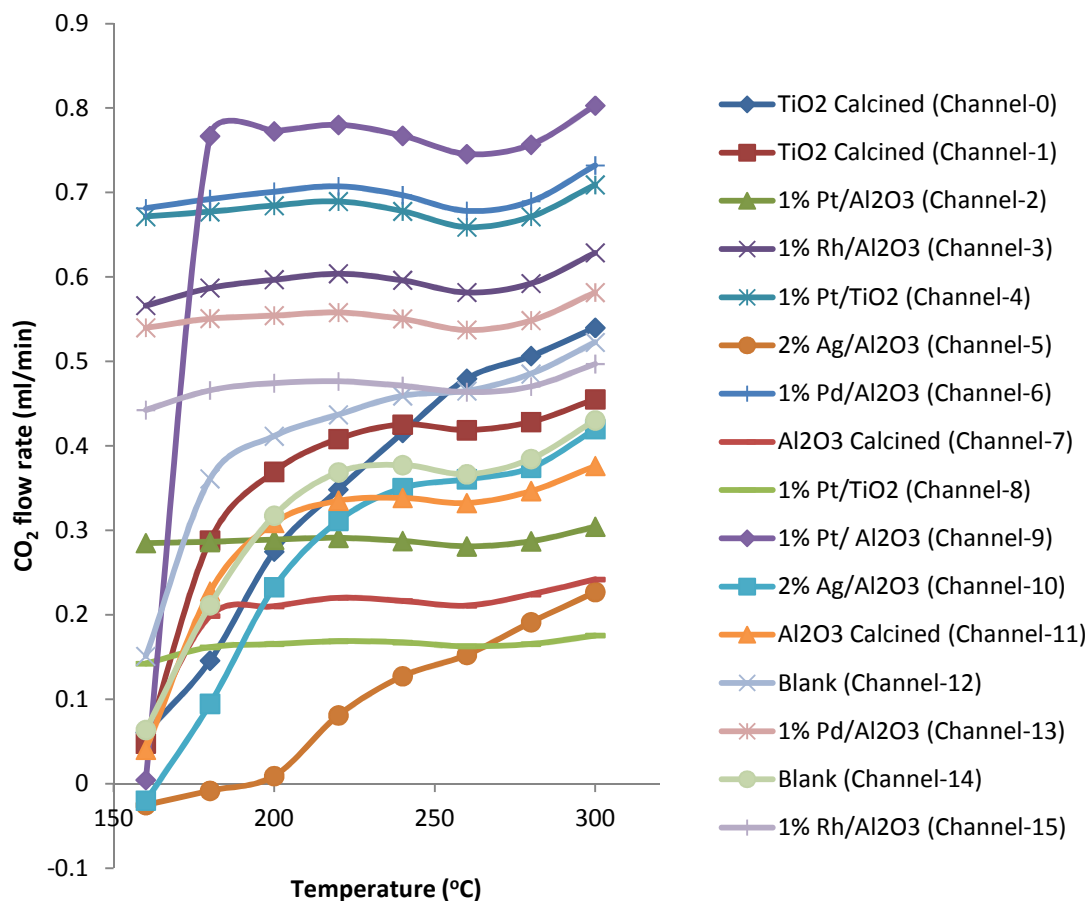
Figure-3.7: The result of CO oxidation for a single run.

This finding was further validated by measuring the flow rate of individual channels before and after loading quartz wool as shown in Figure-3.8. From the Figure-3.8, it was clear that flow rate of most of the channels changed before and after loading quartz wool. This also led to the conclusion that flow rate during calibration and reaction was not the same and hence the calibration was not valid to study the reaction. In addition thermocouples were not placed to monitor the temperature of individual channels. Only one thermocouple attached in between channels 5, 6, 9 and 10 was used to monitor temperature and provide feedback to the temperature controller. As a result, it was very

difficult to keep the temperature constant at the set point and take multiple readings. So the readings were assumed to be taken at the mean temperature.
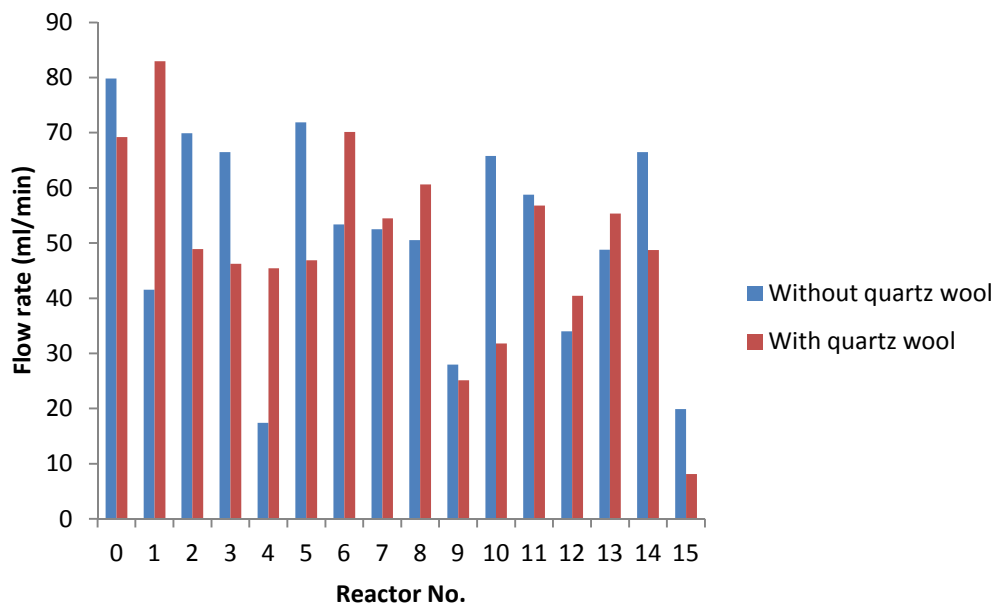
Figure-3.8: Flow rate distribution among the channels before and after loading quartz wool.

The only solutions to these issues were to work on a different reactor of 16 channels having physical separation to prevent crosstalk of flow and temperature. Therefore, this reactor was excluded from any further study.

3.2.3. Conclusion

The PSR was used to study the CO oxidation reaction. The calibration of CO and CO_2 was good because of the uniform distribution of gas mixtures throughout the reactor during calibration. The reaction results were not satisfactory because of the crosstalk of temperature, back mixing of the product gases and flow rate redistribution among the channels. The SSR with 16 separate parallel reactor channels might be a better choice to

pursue this study, because in the SSR, each reactor tube is fitted with thermocouple for individual reactor temperature monitoring. Small diameter (0.01in) capillaries are placed before each reactor channel to ensure similar flow rates through each reactor tube and to prevent back mixing of the product gases.

CHAPTER 4

Results and Discussion of secondary screening reactor study

4.1. Calibration study

Calibrations used in SSR study are discussed in this section. Both univariate and multivariate calibration was employed to study the result of NH_3 SCR of NO. The calibrations and validation of those calibrations are discussed in this section.

4.1.1. Effect of integration time on Calibration

Univariate calibration was used to investigate the effect of integration time on NO calibration. Two different integration times i.e. 0.046375msec and 0.062125msec were used. The objective of this investigation was to improve the lower limit of detection (LLD) and lower limit of quantification of any IR active molecule [86].

PCR, PLS-1, PLS-2 and area based JAIMP methods were used to develop the calibration of NO. The NO calibration curves developed by PLS-1 method (integration time 0.046375msec and offset 240) for all 16 reactors were straight lines with R^2 value $\approx$ 0.94 – 0.99. This calibration was validated by the prediction of a sample of known concentration as shown in Figure-4.1. 66ppm NO in N_2 (Horizontal line in Figure-4.1) was used as the unknown sample to validate the calibration model. The prediction based on the calibration developed by PLS-1 method determined an average NO concentration of 57ppm with a standard deviation of 20ppm.

Figure-4.1: Validation of the NO calibration model for integration time 0.046375msec.

The NO calibration curves developed by PLS-1 method (integration time 0.062125msec and offset 245) for all 16 reactors were also straight lines with R^2 value ≈ 0.95 – 0.99. This calibration was validated by the prediction of a sample of known concentration as shown in Figure-4.2. 66ppm NO in N_2 (Horizontal line in Figure-4.2) was used as the unknown sample to validate the calibration model. The prediction based on the calibration developed by PLS-1 method determined an average 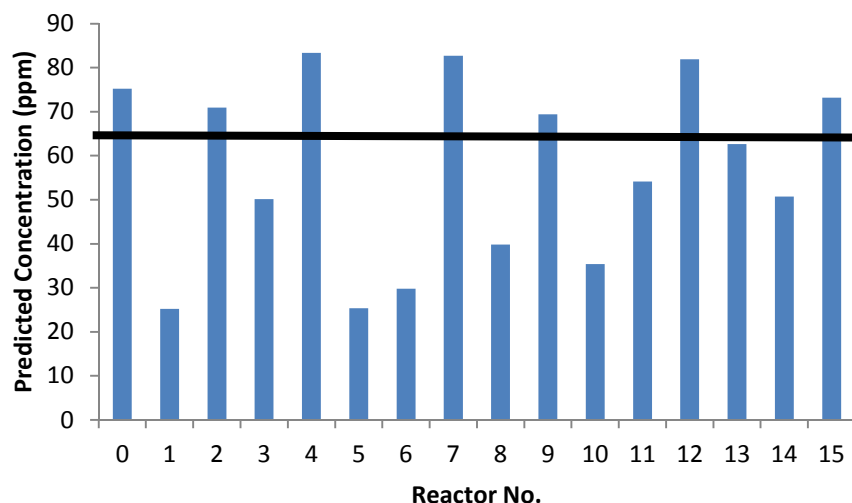NO concentration of 59ppm with a standard deviation of 6ppm. Calibration developed with integration time 0.062125msec showed better predictions with small standard deviation and was used for further studies.
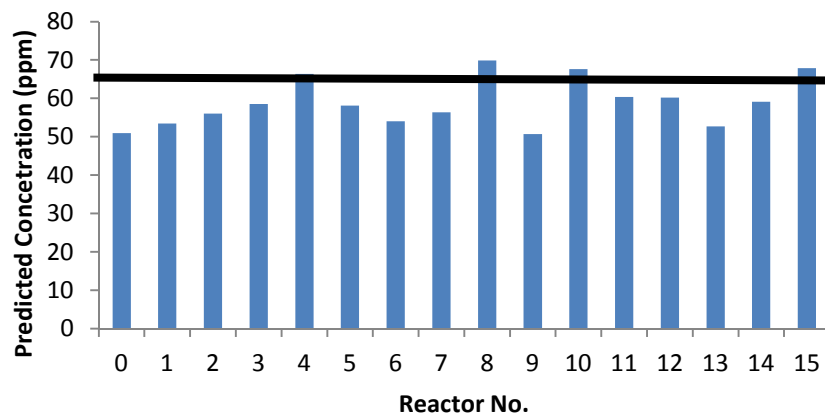
Figure-4.2: Validation of the NO calibration model for integration time 0.062125msec.

4.1.2. Univariate calibration for Ammonia (NH₃)

The IR spectrum of NH$_3$ shown in Figure-4.3 has three distinct types of vibrational modes: symmetric and asymmetric bending and stretching. Stretching mode overlaps with the stretching vibration modes of H$_2$O and asymmetric bending mode overlaps with the bending mode of H$_2$O and the asymmetric stretching mode of NO$_2$. However, the symmetric bending vibration mode peak of NH$_3$ does not overlap with any other IR active species.
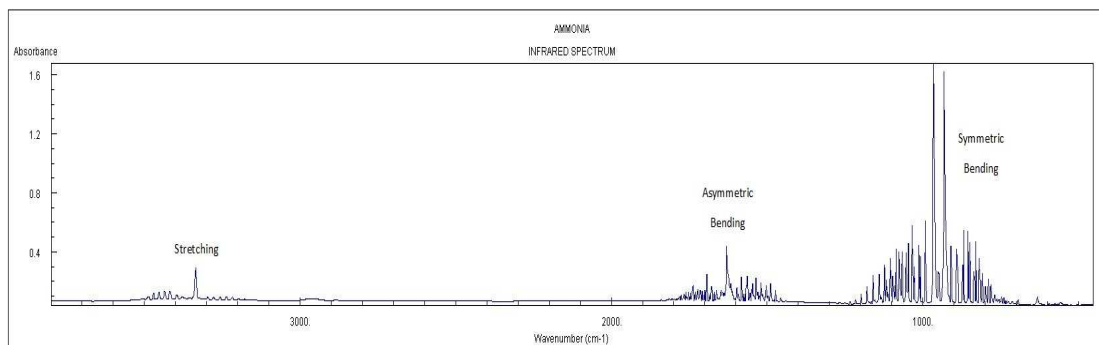
Figure-4.3: IR spectrum of NH₃ (Reproduced from NIST Webbook).

Since this peak is close to the detection limit of ZnSe windows, a portion of that peak area was used to develop a calibration of NH_3 in GRAMS. The reason behind choosing a portion of the peak instead of the complete peak is that, close to wavenumber cutoff region of the ZnSe windows signal to noise ratio is very high. PLS-1 method was used to develop the univariate calibration of NH_3 in the concentration range of 0 to 1500ppm. The calibration curves for all 16 reactors were straight lines with $R^2$ value $\approx$ 0.94 – 0.99. This calibration was validated by the prediction of 153ppm NH_3 in N_2. The prediction based on the calibration determined an average NH_3 concentration of 131ppm with a standard deviation of 46ppm.

4.1.3. Multivariate calibration for Nitric Oxide (NO) and water (H_2O)

PLS-1 method was used to develop the multivariate calibration for NO and H_2O. The NO calibration curves for all 16 reactors were straight lines with R^2 value $\approx$ 0.95 – 0.98, whereas, H_2O calibration curves for all 16 reactors were also straight lines with R^2 value $\approx$ 0.87 – 0.95.

This calibration was validated by the prediction of samples of known concentration as shown in Figure-4.4. The predicted concentrations are given below in Table-4.1. The difference between expected and predicted concentration based on the calibration was 5 - 44ppm for NO and 0.1 – 0.6% for H_2O.

Table-4.1: Predicted concentrations of NO and H$_2$O

Actual concentration	Predicted concentration	
0% H$_2$O 156ppm NO	H$_2$O (%)	0.3 ± 0.2
	NO (ppm)	172 ± 26
0% H$_2$O 1102ppm NO	H$_2$O (%)	0.5 ± 0.2
	NO (ppm)	1089 ± 31
2% H$_2$O 156ppm NO	H$_2$O (%)	2.1 ± 0.4
	NO (ppm)	141 ± 34
2% H$_2$O 1102ppm NO	H$_2$O (%)	1.8 ± 0.5
	NO (ppm)	1107 ± 29
4% H$_2$O 156ppm NO	H$_2$O (%)	4.1 ± 0.1
	NO (ppm)	112 ± 58
4% H$_2$O 1102ppm NO	H$_2$O (%)	4.3 ± 0.3
	NO (ppm)	1097 ± 23
5.5% H$_2$O 156ppm NO	H$_2$O (%)	4.9 ± 0.3
	NO (ppm)	182 ± 77
5.5% H$_2$O 1102ppm NO	H$_2$O (%)	5.4 ± 0.2
	NO (ppm)	1119 ± 35
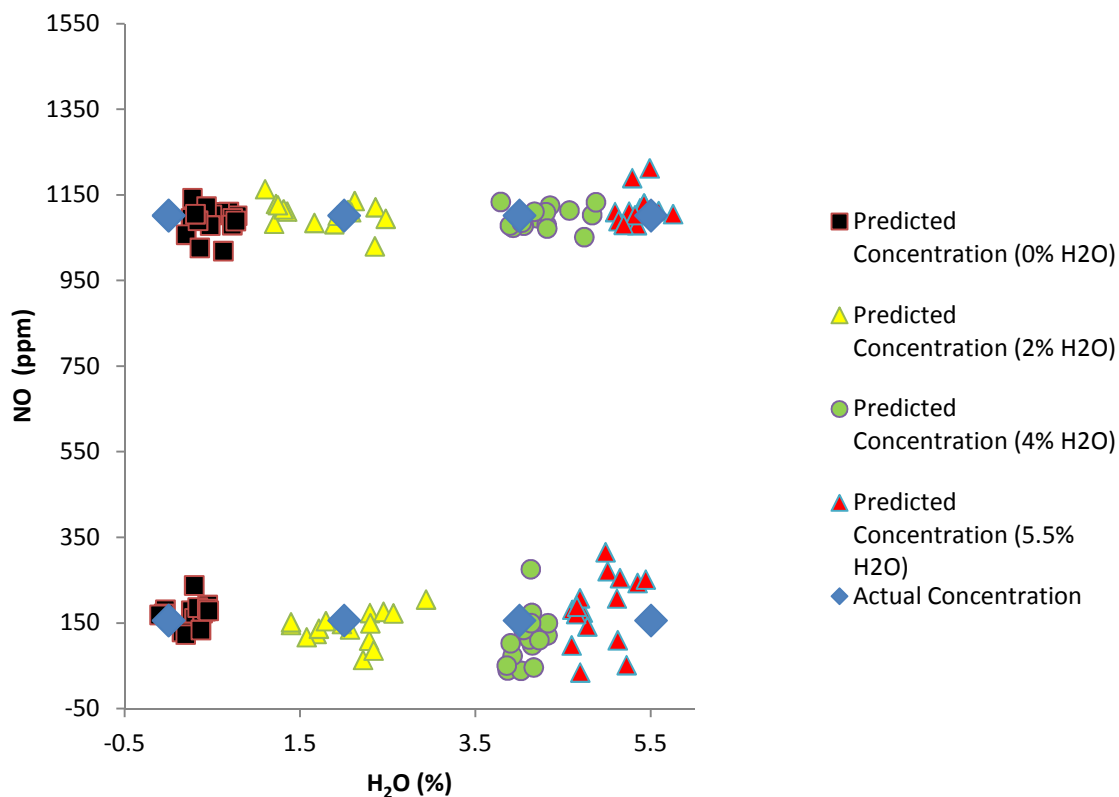
Figure-4.4: Validation of the multivariate calibration model.

4.2. Reactor study

Reactions carried out in SSR are discussed in this section. NH_3 SCR of NO was studied in SSR with or without H_2O injection. Results of those reaction studies are discussed in this section.

4.2.1. Nitric Oxide Reduction without water injection

NH_3 SCR of NO without H_2O injection was used as the benchmark reaction to validate the SSR. Titania-vanadia was chosen as the catalyst for NH_3 SCR of NO. The NO conversion of titania-vanadia is 80-90% at 300-450°C [55, 57-58]. Twelve reactors (Reactor no. 1-6, 9-14) were loaded with titania-vanadia and four reactors (Reactor no. 0,

7, 8, 15) were left blank during the study. The flow rate distribution among the channels is shown in Figure-4.5. The average flow rate was 116.6sccm with a standard deviation of 20.4sccm.
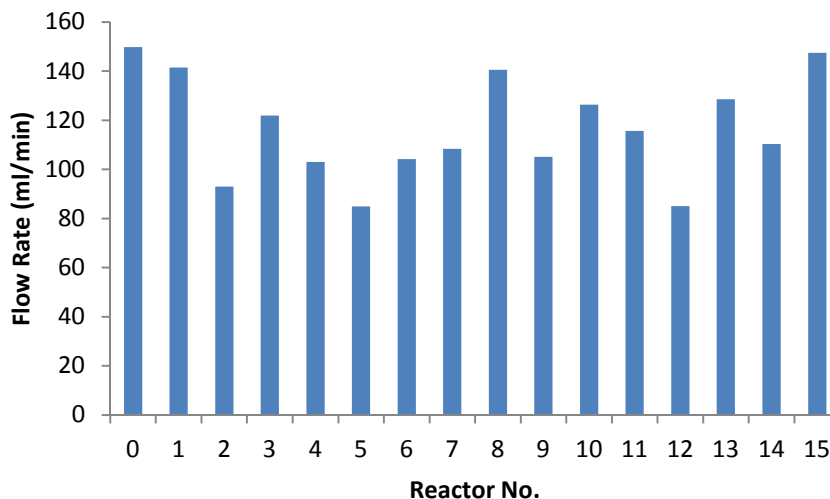
Figure-4.5: Flow rate distribution among the reactors.

The reaction was studied at 150°C, 250°C, 350°C and 450°C for both ramps up and down of temperature. NO conversion in reactor-5 for both studies is shown below in Figure-4.6 as an example. During ramp up, NO conversion was very low at 150°C (16.08 $\pm$ 5.01%). NO conversion increased with the increase of temperature and reaches maximum at 350°C (104.27 $\pm$ 2.99%). Above 350°C NO conversion starts to decrease, but NO conversion is still > 80% at 450°C which is in agreement with the literature [55, 57-58]. During ramp down, NO conversion was > 80% at 450°C. NO conversion increased with the decrease of temperature and reaches maximum at 350°C (111.01 $\pm$ 1.88%). Upon further decrease NO conversion starts to decrease and reaches minimum at

$150^{o}C$ ($18.88 \pm 0.7\%$). The variation in NO conversion observed at different temperatures is within the experimental error.
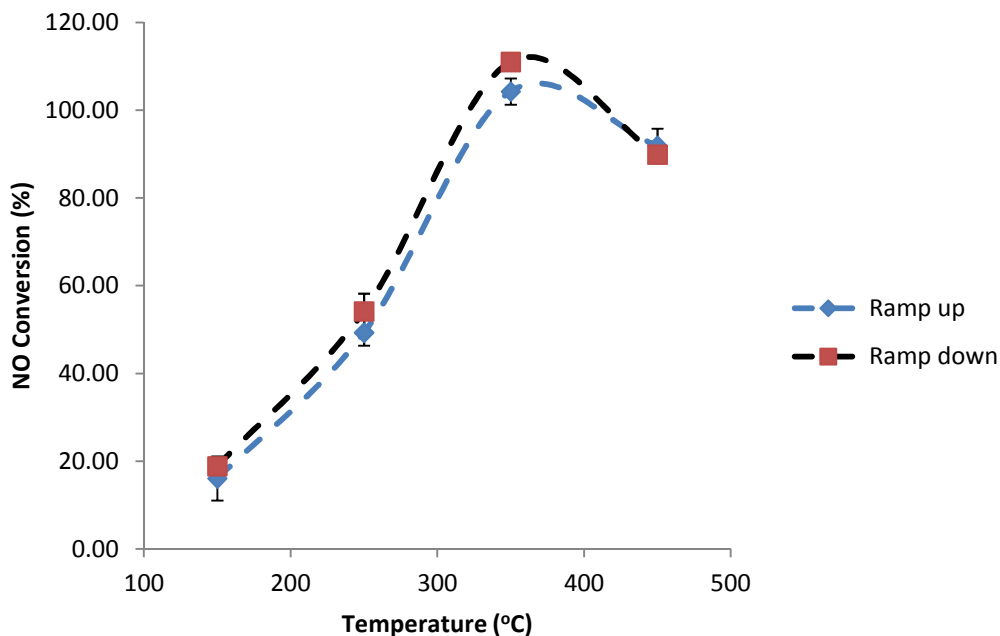
Figure-4.6: NO conversion in reactor-5.

The main reason of SSR study was to check the reproducibility of the NO conversion result by comparing the NO conversion in different reactors loaded with titania-vanadia at different temperatures. NO conversion for both studies is given below in Figure-4.7. Both ramp up and ramp down studies followed the same trend as was observed in case of reactor-5. The standard deviation shown at different temperatures might be a result of titania-vanadia not being a homogeneous catalyst. Titania-vanadia (commercial) monolith catalyst was crushed to powder (not sieved) and used in these studies. Therefore, the nonhomogeneous titania-vanadia catalyst showed some variation in NO conversion at different temperatures which is displayed as the error bars in Figure-4.7. However, NO conversion was > 80% at $350^{o}C$ and $450^{o}C$ for all reactors containing

titania-vanadia catalyst. This validates the effectiveness of the SSR. Some NO conversion was also observed in the blank reactors. Stainless steel being a weak catalyst of NH_3 SCR of NO might be reason behind this conversion. The variation in NO conversion observed in different blank reactors might be consequence of different flow rates in different blank reactors.
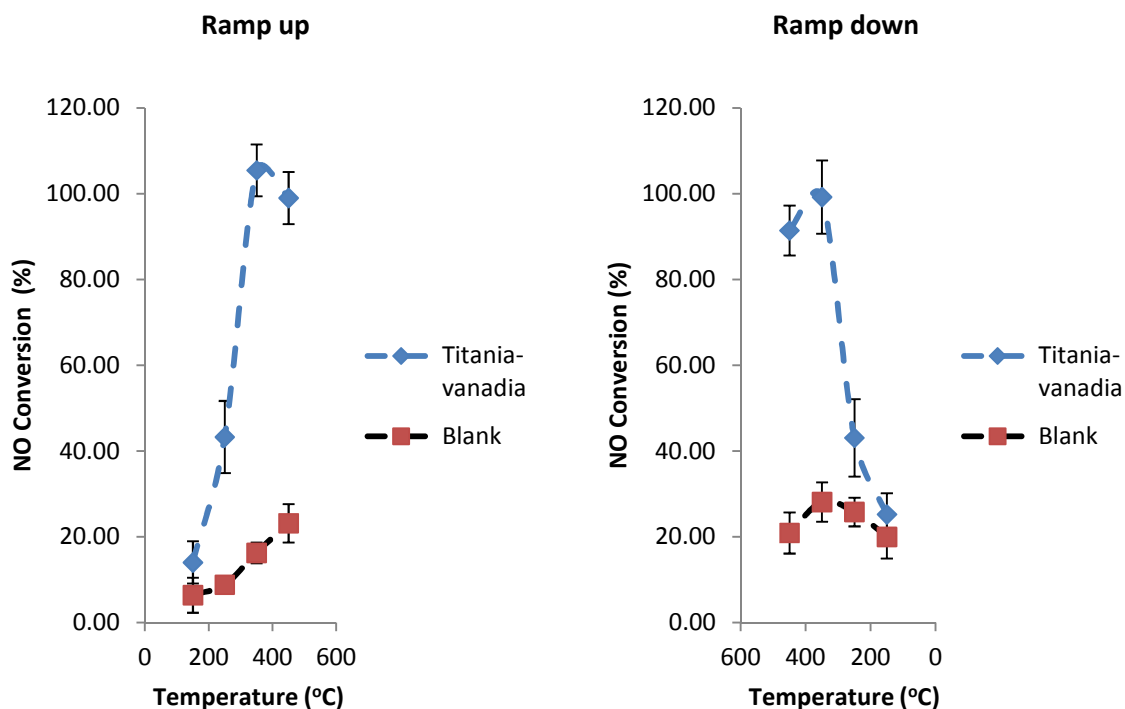
Figure-4.7: NO conversion at 150°C, 250°C, 350°C and 450°C.

There is a weak relationship between flow rate and NO conversion at 150°C and 250°C in reactors loaded with titania-vanadia. Generally, if the flow rate is small, NO and NH_3 residence time on the catalyst bed is high which results in high NO conversion. This is evident in Figure-4.8 shown below. As sown in Figure-4.8 the relationship is stronger at 250°C than the 150°C.
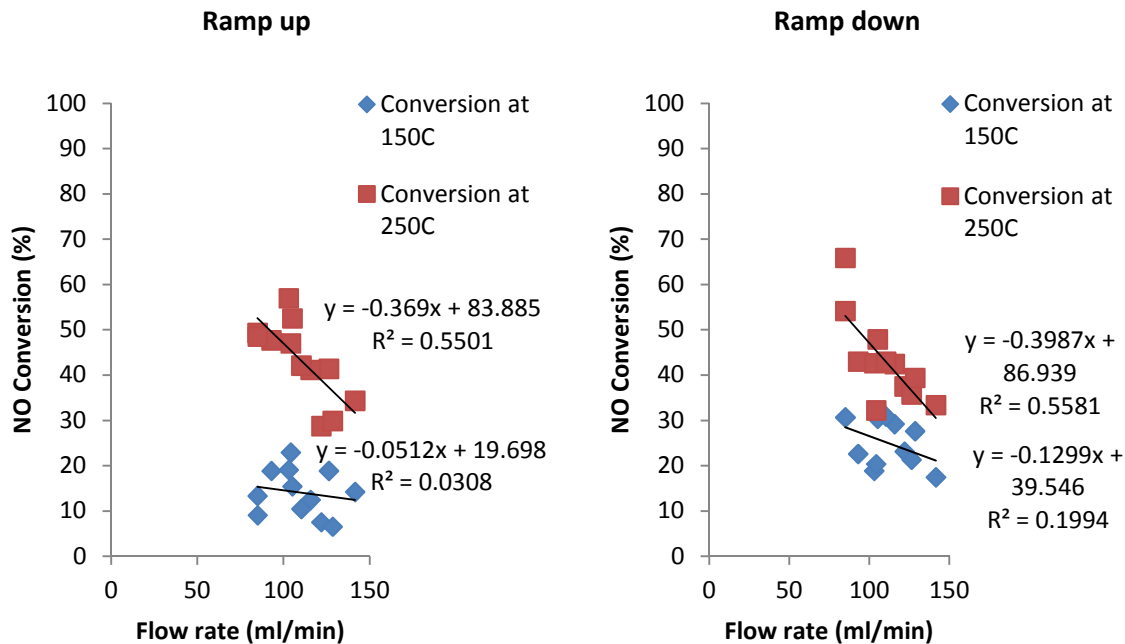
Figure-4.8: Relationship between flow rate and NO conversion at 150°C and 250°C.

NH$_3$ conversion was also determined for the above studies. NH$_3$ conversion in reactor-14 for both studies is given below in Figure-4.9 as an example. During ramp up, NH$_3$ conversion was very low at 150°C (3.94 ± 4.78%). NH$_3$ conversion increased with the increase of temperature and reaches maximum at 350°C (95.43 ± 5.06%). Above 350°C NH$_3$ conversion starts to decrease, but NH$_3$ conversion is still > 80% at 450°C. During ramp down, NH$_3$ conversion increased with the decrease of temperature and reaches maximum at 350°C (87.57 ± 3.96%). Upon further decrease NH$_3$ conversion starts to decrease and reaches minimum at 150°C (0.79 ± 3.75%). The variation in NH$_3$ conversion observed at different temperatures is within the experimental error.
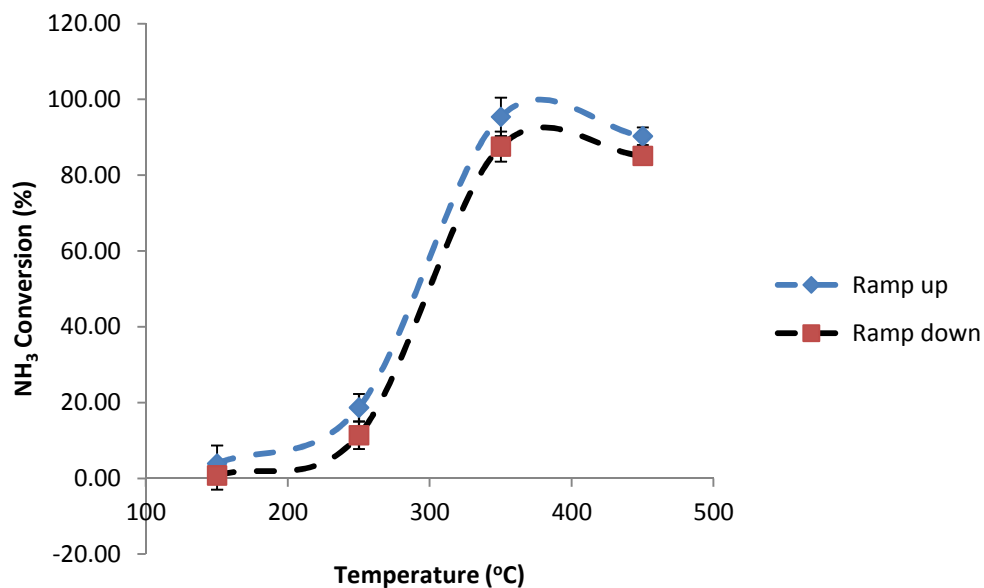
Figure-4.9: NH$_3$ conversion in reactor-14.

NH$_3$ conversion in all the reactors was also studied for both ramp up and down of temperature and shown below in Figure-4.10. Both ramp up and ramp down studies followed the similar trend as was observed in case of reactor-14. In case of NH$_3$ conversion, high standard deviations were observed due to NH$_3$ symmetric bending mode peak being close to wavenumber cutoff region ($\sim$ 900cm^{-1}). However, NH$_3$ conversion at 350°C and 450°C was > 80%, which is in agreement with the stoichiometry of the reaction (1.17).
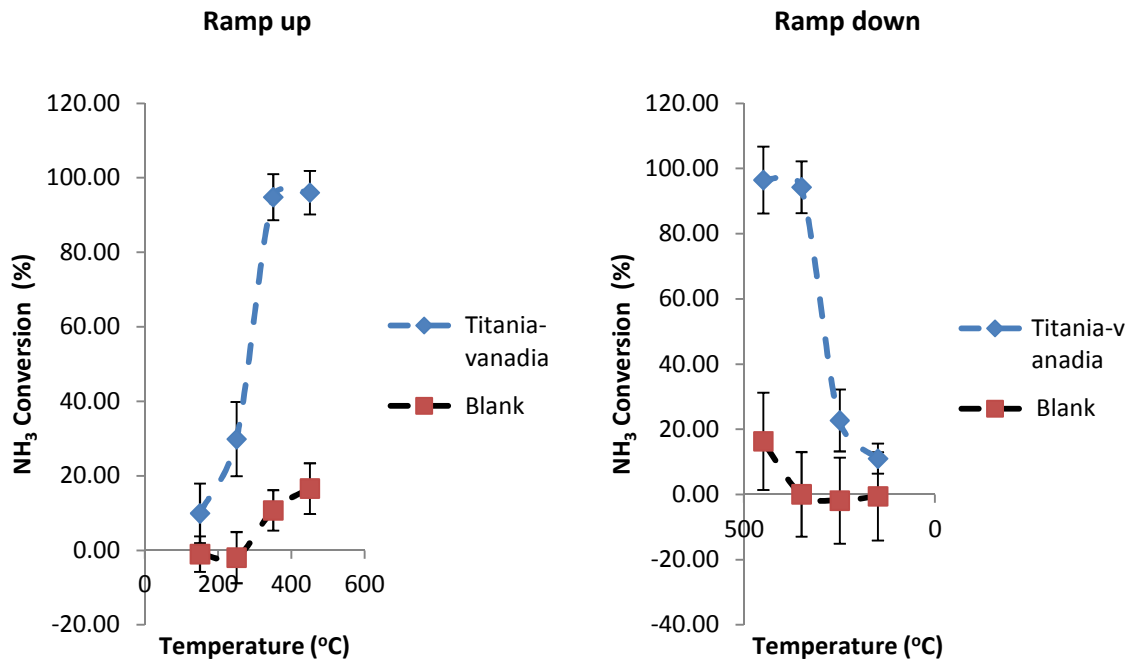
Figure-4.10: NH$_3$ conversion at 150°C, 250°C, 350°C and 450°C.

4.2.2. Nitric Oxide Reduction with water injection

NH$_3$ SCR of NO with H$_2$O injection was also studied in the SSR with titania-vanadia in twelve reactors (Reactor no. 1-6, 9-14) and four blank reactors (Reactor no. 0, 7, 8, 15). The reaction was studied at 150°C, 250°C, 350°C and 450°C. NO and NH$_3$ conversion in reactor-2 is shown below in Figure-4.11 as an example. NO and NH$_3$ conversion was very low at 150°C. NO and NH$_3$ conversion increased with the increase of temperature and reaches maximum at 450°C. At 450°C NO conversion was 97.38 $\pm$ 5.77% and NH$_3$ conversion was 98.65 $\pm$ 2.72%, which is in agreement with the stoichiometry of the reaction (1.17).
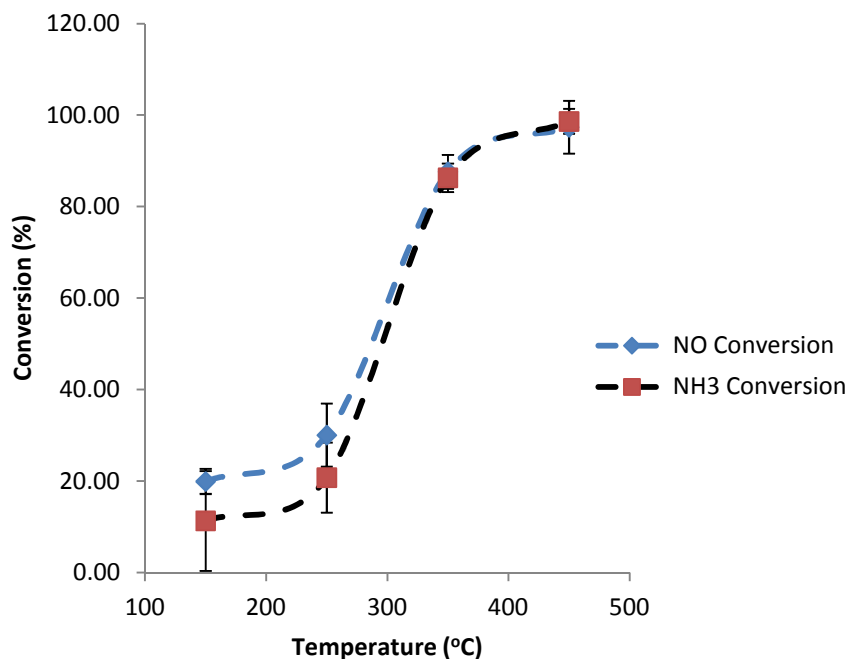
Figure-4.11: NO and NH$_3$ conversion in reactor-2.

Reproducibility behavior was also studied in this study. NO and NH$_3$ conversion for this study is shown below in Figure-4.12. Both NO and NH$_3$ conversion followed the similar trend as was observed in case of reactor-2. It was observed that, NO and NH$_3$ conversion was low in case of H$_2$O injection. This might be a result of the deactivation of the catalysts due to aging (~5 days) of the catalysts in the reactors. High standard deviations were observed in case of NH$_3$ conversion due to NH$_3$ symmetric bending mode peak being close to wavenumber cutoff region (~ 900cm^{-1}). The signal to noise ratio being high in that region introduces this error.

NO Conversion NH_3 Conversion
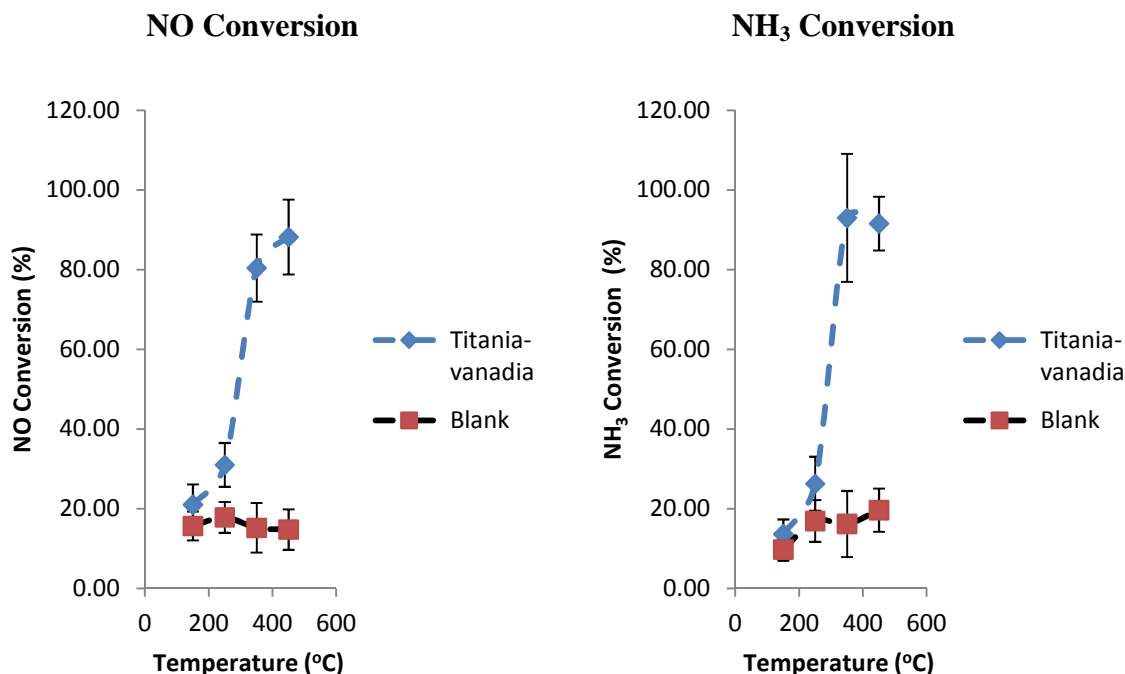
Figure-4.12: NO and NH_3 conversion at 150^oC, 250^oC, 350^oC and 450^oC.

4.2.3. High Throughput Catalyst Screening

A high throughput catalyst screening was performed for NH_3 based SCR of NO with H_2O injection in SSR. During the screening 25 metal promoted zeolite catalysts were tested in 3 batches. Cu-Zeolite beta (Cu-Zeolite-BEA) was used as the reference catalyst for these tests. The results of these tests are described below.

In the first batch Ag, Ba, Ce, Co, Cu, Fe, Mn, Ni, Sn and Zn promoted Zeolite-BEA catalysts were tested at 550^oC, 450^oC, 350^oC, 250^oC and 150^oC. After fresh evaluation of the catalysts a hydrothermal treatment was carried out at 750^oC for 16hours. Then catalysts were tested again at 550^oC, 450^oC, 350^oC, 250^oC and 150^oC. For Cu-Zeolite-BEA, NO conversion was very low at 550^oC (0%). NO conversion increased with the

decrease of temperature and reached maximum at 250°C. After 250°C, NO conversion started to decrease, but NO conversion was 65% at 150°C. After hydrothermal treatment NO conversion followed the same trend, but NO conversion was much higher after hydrothermal treatment as shown in Figure-4.13. On the other hand, NH$_3$ conversion was ~100% at 550°C-250°C before and after hydrothermal treatment. At high temperature NH$_3$ oxidizes and forms NO$_x$ which results in high NH$_3$ conversion and low NO conversion [65].
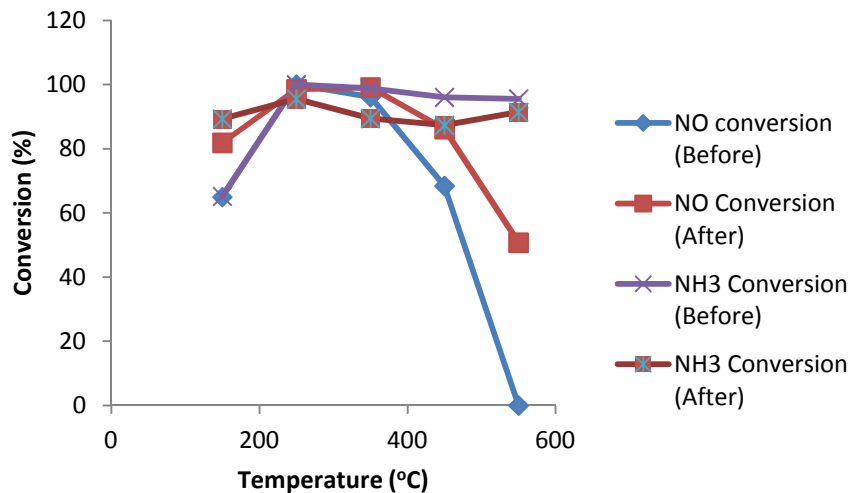
Figure-4.13: NO and NH$_3$ conversion on Cu-Zeolite-BEA before and after hydrothermal treatment.

N$_2$O production was also studied for Cu-Zeolite-BEA. Before hydrothermal treatment higher N2O production was observed at 450°C, while after hydrothermal treatment higher N2O production was observed at 250°C as shown in Figure-4.14.
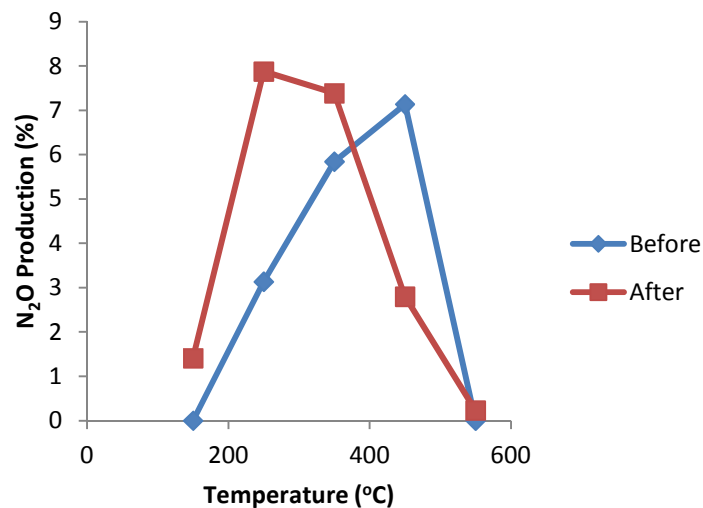
Figure-4.14: N₂O production on Cu-Zeolite-BEA before and after hydrothermal treatment.

Among the other catalysts tested in batch-1, Ag, Ba, Mn, Ni and Zn promoted Zeolite-BEA catalysts showed high NO conversion at $450^{o}C$ (> 60%) while Co, Fe and Sn promoted Zeolite-BEA catalysts showed high NO conversion at $350^{o}C$ as shown in Figure-4.15.
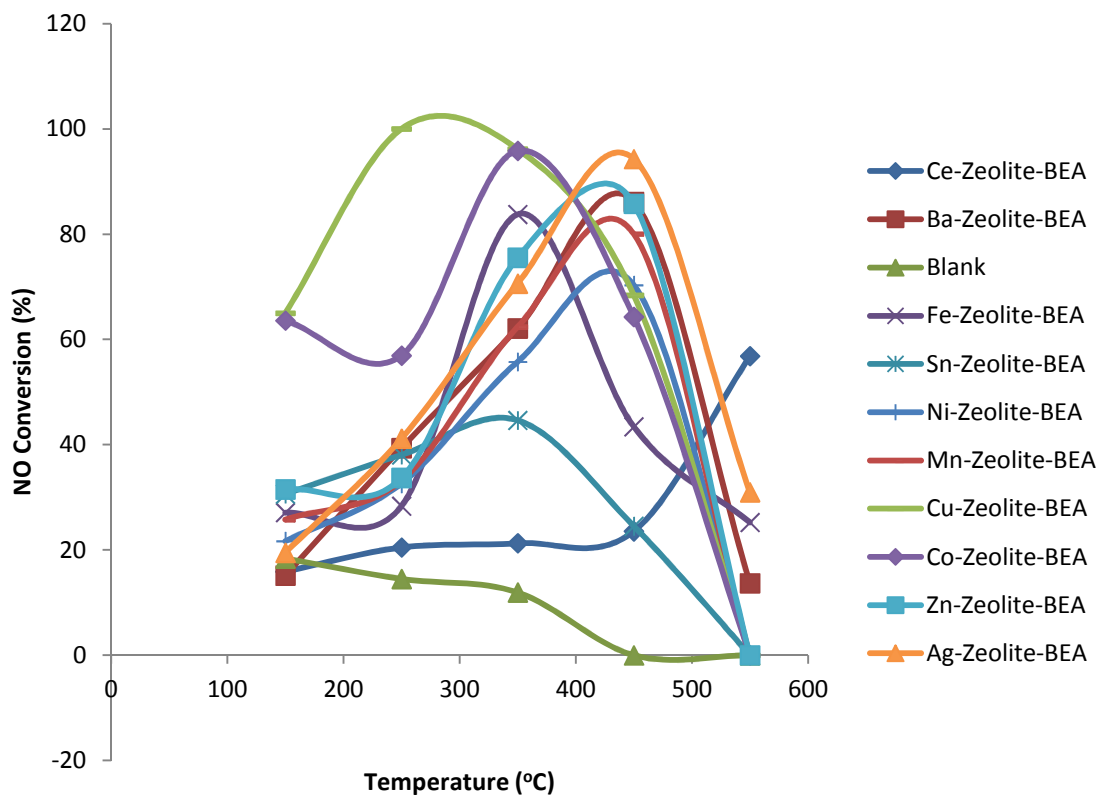
Figure-4.15: NO conversion on metal promoted Zeolite-BEA catalysts.

After hydrothermal treatment, Ag, Ba, and Zn promoted Zeolite-BEA catalysts showed high NO conversion at 450°C while Mn and Ni promoted Zeolite-BEA catalysts showed high NO conversion at 350°C as shown in Figure-4.16. After hydrothermal treatment, some channels were plugged due to the formation of ammonium nitrate in the reactors and/or capillary tubing. Hence the performance of some catalysts was not possible to be determined.
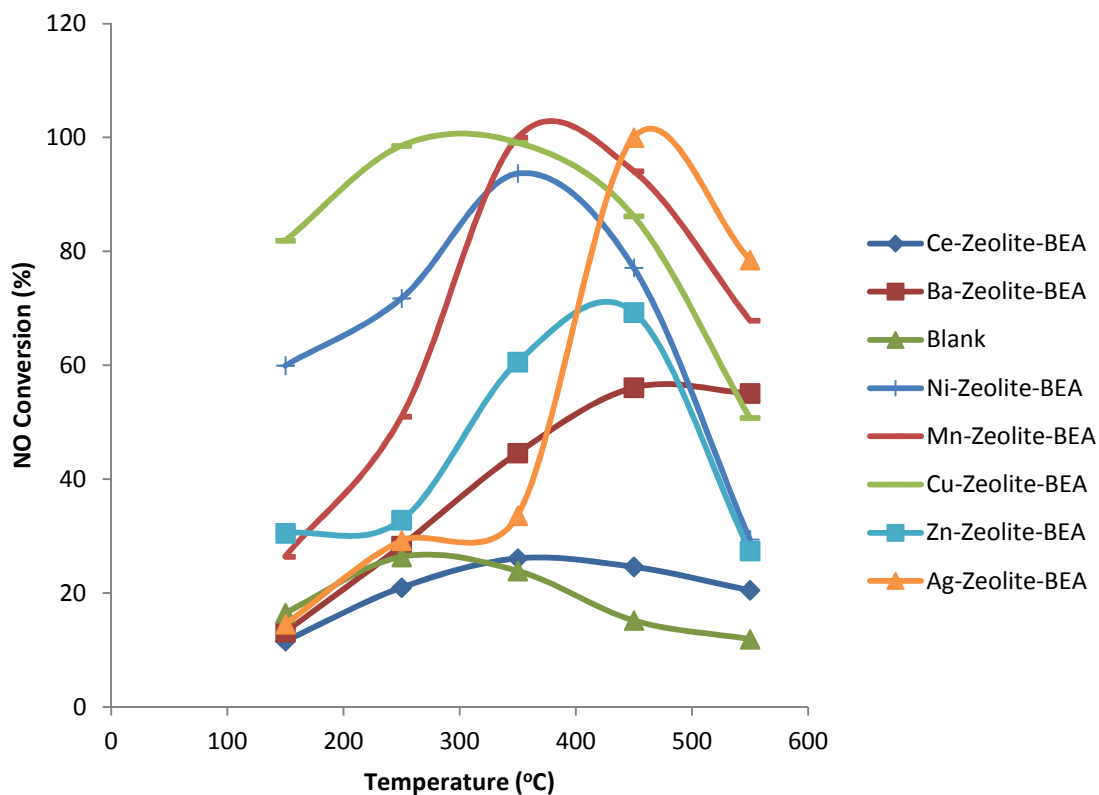
Figure-4.16: NO conversion on metal promoted Zeolite-BEA catalysts after hydrothermal treatment.

In the second batch Ag, Cu, Gd, In, La and Nd promoted Zeolite-BEA and Cu promoted ZSM-5 catalysts were tested. Cu-Zeolite-BEA showed similar activity before and after hydrothermal treatment. Among the other catalysts tested in batch-2, Ag, Gd, In and La promoted Zeolite-BEA, Cu-ZSM-5 (23:1) and Cu-ZSM-5 (80:1) catalysts showed high NO conversion at $350^{o}C$ - $450^{o}C$ while Cu-ZSM-5 (30:1) catalyst showed high NO conversion at $250^{o}C$ as shown in Figure-4.17. Nd-Zeolite-BEA and Cu-ZSM-5(200-400:1) did not show good NO conversion.

Figure-4.17: NO conversion on metal promoted Zeolite catalysts (Batch-2).

After hydrothermal treatment, some channels were plugged again due to the formation of ammonium nitrate in the reactors and/or capillary tubing. Hence the performance of some catalysts was not possible to be determined. The NO conversion on rest of the catalysts was low as shown in Figure-4.18. A reason behind this might be the long hydrothermal treatment period due to the failure of the temperature controller.
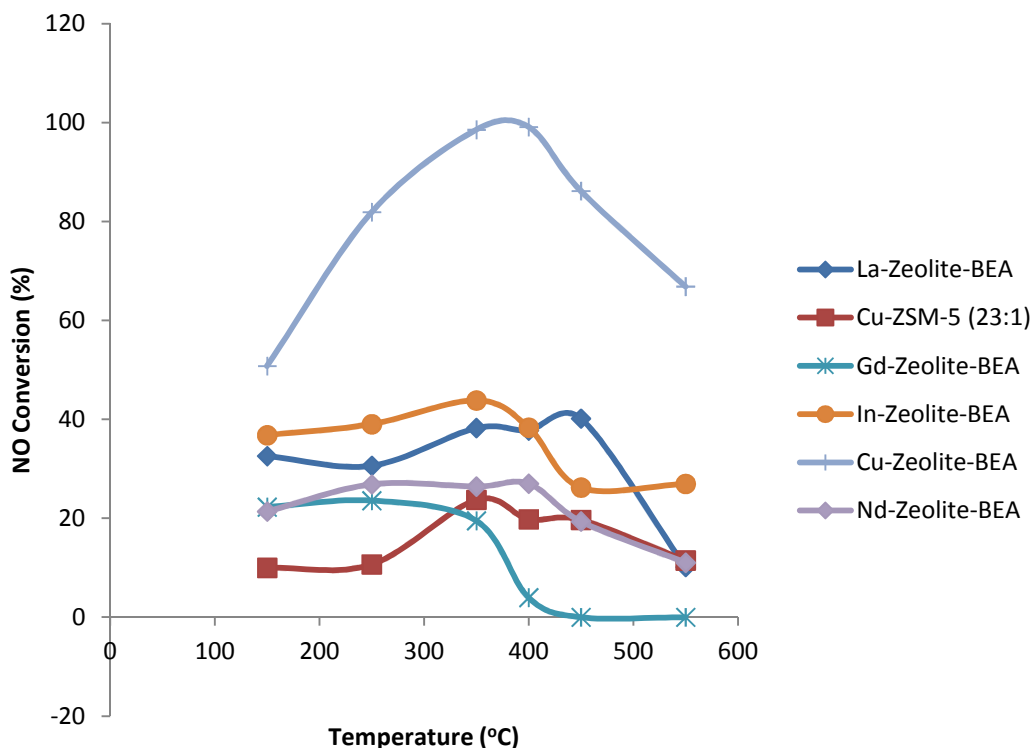
Figure-4.18: NO conversion on metal promoted Zeolite catalysts (Batch-2) after hydrothermal treatment.

In the third batch Cu-Zeolite-BEA, Cu-ZSM-5 (80:1), Cu-SSZ-13, Fe-SSZ-13, Cu-Ag-SSZ-13, Cu-Ba-SSZ-13, Cu-Fe-SSZ-13, Cu-La-SSZ-13 and Cu-Mn-SSZ-13 catalysts were tested. Cu-Zeolite-BEA showed similar activity before and after hydrothermal treatment. Among the other catalysts tested in batch-3, Cu-SSZ-13, Fe-SSZ-13, Cu-Ag-SSZ-13, Cu-Fe-SSZ-13, Cu-La-SSZ-13 and Cu-Mn-SSZ-13 catalysts showed high NO$_x$ conversion at 250°C - 450°C while Cu-ZSM-5 (80:1) catalyst showed high NO$_x$ conversion at 350°C – 450°C as shown in Figure-4.19. Cu-Ba-SSZ-13 did not show good NO conversion.
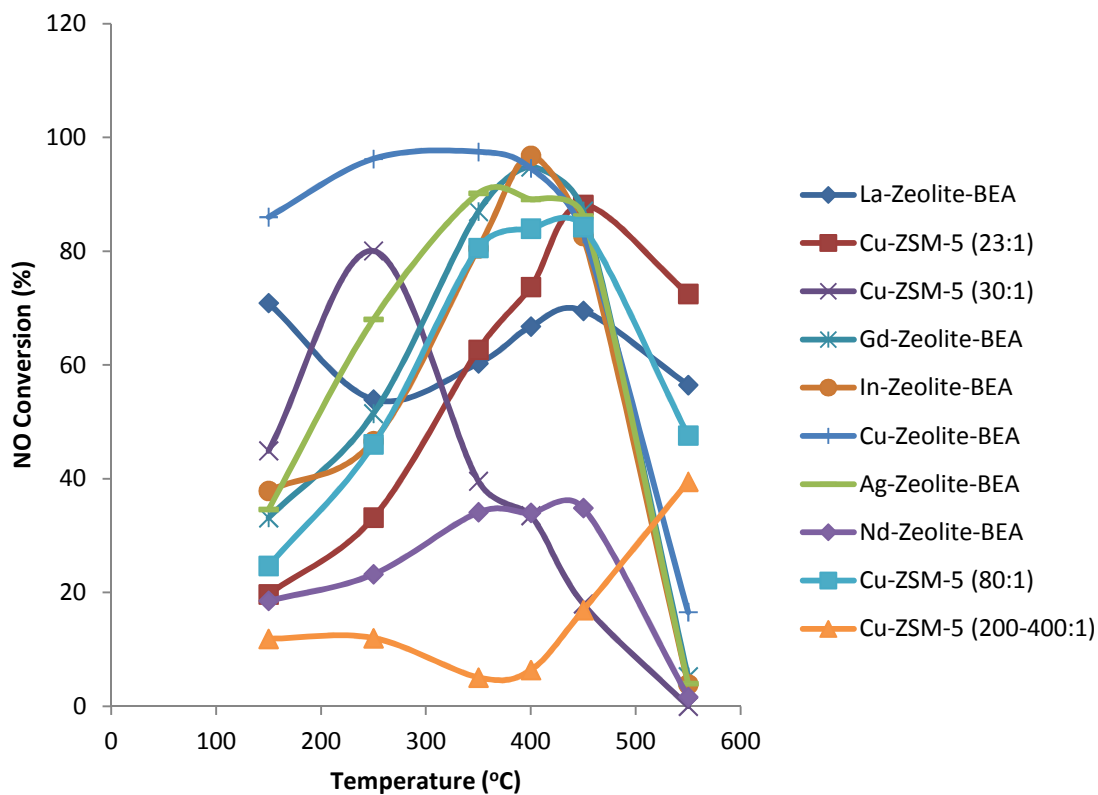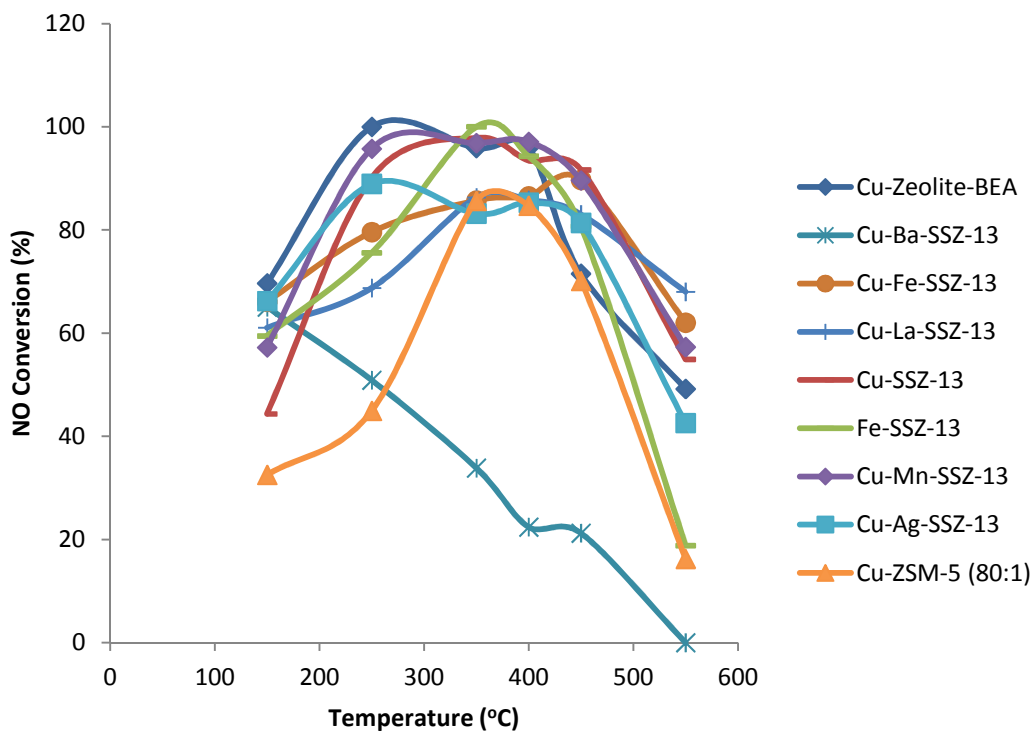
Figure-4.19: NO conversion on metal promoted Zeolite catalysts (Batch-3).

After hydrothermal treatment, most of the channels were plugged due to the formation of ammonium nitrate in the reactors and/or capillary tubing and the pressure drop rose to 90psig. 10 Capillary tubing were changed to decrease the pressure drop to 22psig. NO conversion on all the catalysts was almost same as before hydrothermal treatment (Figure-4.20).
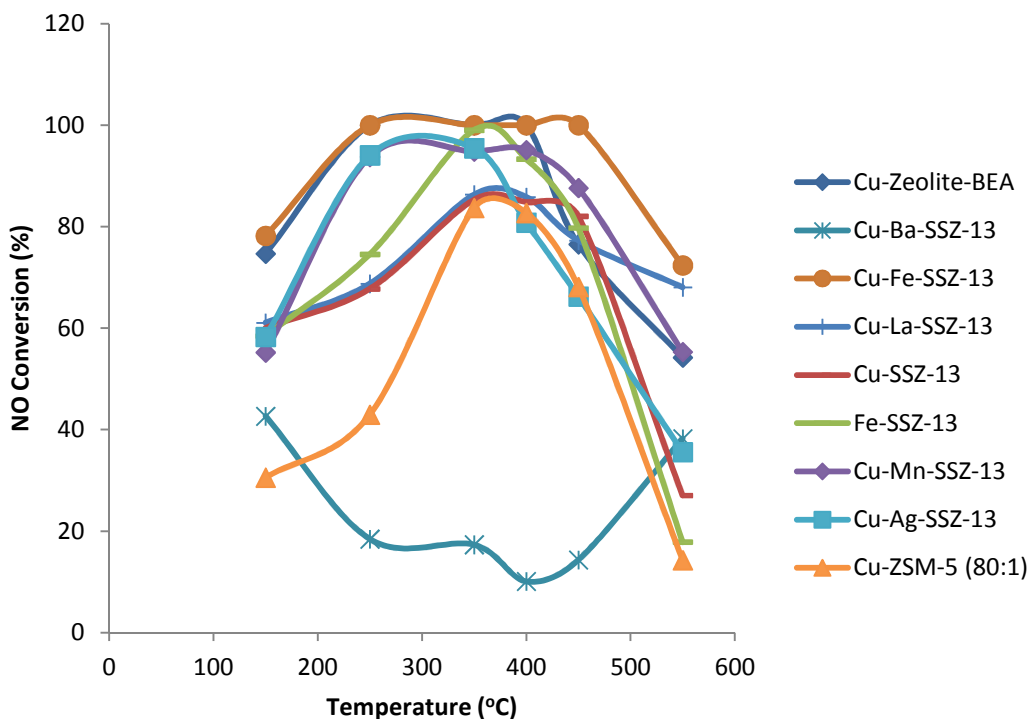
Figure-4.20: NO conversion on metal promoted Zeolite catalysts (Batch-3) after hydrothermal treatment.

4.2.4. Conclusion

SSR was used to study NH_3 SCR of NO reactions with or without H_2O injection. Multivariate calibration of NO and H_2O and univariate calibration of NH_3 and N_2O was developed to determine NO and NH_3 conversion and N_2O production respectively. It was observed that, NO and NH_3 conversion on titania-vanadia at 350^oC and 450^oC was > 80%, which is in agreement with the literature [55, 57-58]. This proves the stoichiometry of the reaction and validates the effectiveness of the SSR. SSR was also used to study 25 metal promoted zeolite catalysts. Cu-Zeolite-BEA, Ag-Zeolite-BEA, Cu-SSZ-13, Fe-SSZ-13, Cu-Ag-SSZ-13, Cu-Fe-SSZ-13, Cu-La-SSZ-13 and Cu-Mn-SSZ-13 catalysts showed good NO conversion at $250-450^oC$ and can be a good SCR catalyst.

CHAPTER 5

Conclusion and Future works

5.1. Conclusion

NH_3 based SCR of NO is an important reaction in automobiles in the context of air pollution. As the EPA regulation becomes more stringent the necessity to reduce NO_x in oxidizing atmosphere becomes more challenging. This drives the discovery of new catalyst for NH_3 based SCR of NO. New catalysts are continuously tested under different flue gas condition to meet the requirements of EPA. HTR (e.g. SSR) allows us to study multiple catalysts at the same condition and facilitates the discovery of new catalyst.

In this research two HTR systems were studied. CO oxidation study performed in PSR enabled us to understand the design criteria of practical HTR system devoid of crosstalk and back mixing of product gas. On the other hand, NH_3 based SCR of NO reactions with or without H_2O injection was studied using SSR. Multivariate calibration of NO and H_2O and univariate calibration of NH_3 was employed to determine NO and NH_3 conversion respectively. NO and NH_3 conversion on titania-vanadia at 350^oC and 450^oC was $> 80\%$, which proves the stoichiometry of the reaction and validates the effectiveness of the SSR. 25 metal promoted zeolite catalysts were also studied. Cu-Zeolite-BEA, Ag-Zeolite-BEA, Cu-SSZ-13, Fe-SSZ-13, Cu-Ag-SSZ-13, Cu-Fe-SSZ-13, Cu-La-SSZ-13 and Cu-Mn-SSZ-13 catalysts showed good NO conversion at $250\text{-}450^oC$ and can be a good SCR catalyst.

5.2. Upcoming industrial project

SSR will be used to study 50 samples supplied by an industrial company for NH_3 SCR of NO. The catalysts will be tested for long times and their SCR catalytic activity and deactivation will be investigated. The SCR performance of catalysts will be evaluated at 7 different temperatures three times over the entire study. Hydrothermal aging of the catalysts will be performed at elevated temperatures to find out the stability of the catalyst in harsh condition. Inlet and outlet concentration of NO, NO_2, N_2O, NH_3 will be measured to determine the conversion of NO and NH_3 and selectivity of N_2O and NO_2. Temperature and WHSV will also be monitored to check the correlation between flow rate, temperature and conversion in different reactors.

REFERENCES

1. Kaspar, J. et al. (2003). "Automotive catalytic converters: current status and some perspectives." Catalysis Today 77(4): 419-449.

2. Roy, S. et al. (2009). "Catalysis for NO_x abatement." Applied Energy 86(11): 2283-2297.

3. Deka, U. et al. (2013). "Local Environment and Nature of Cu Active Sites in Zeolite-Based Catalysts for the Selective Catalytic Reduction of NO_x." ACS Catalysis 3(3): 413-427.

4. Brandenberger, S. et al. (2008). "The State of the Art in Selective Catalytic Reduction of NO_x by Ammonia Using Metal-Exchanged Zeolite Catalysts." Catalysis Reviews-Science and Engineering 50(4): 492-531.

5. Falcone, D. D. (2010). "Novel Catalyst Screening for Low Temperature NO_x Abatement" Bachelors thesis, University of Delaware.

6. United States Environmental protection Agency. Air Trends. http://www.epa.gov/airtrends/2011/report/airpollution.pdf. (Accessed Sep 15, 2012).

7. Fanson, P. T. (2002). "FTIR analysis of supported catalyst systems related to the reduction of automotive exhaust emissions" Doctoral thesis, Purdue University.

8. Burch, R. and Watling T.C. (1997). "The difference between alkanes and alkenes in the reduction of NO by hydrocarbons over Pt catalysts under lean-burn conditions." Catalysis Letters 43: 19-23.

9. Klingstedt et al. (2004). "A highly active Ag/alumina catalytic converter for continuous HC-SCR during lean-burn conditions: from laboratory to full-scale vehicle tests." Topics in Catalysis 30-1(1-4): 27-30.

10. Bartolomew, C. H. and Farrauto, R. J. (2006). "Fundamentals of Industrial catalytic processes." Second edition, John Wiley & Sons INC.

11. Vijay, R. (2007). "Discovery And Mechanistic Investigation Of NO_x Traps And NH_3 Decomposition Catalysts Using High-Throughput Experimentation." Doctoral thesis, University of Delaware.

12. Burch, R. et al. (2004). "Exceptional activity for NO_x reduction at low temperatures using combinations of hydrogen and higher hydrocarbons on Ag/Al_2O_3 catalysts." Topics in Catalysis 30-1(1-4): 19-25.

13. Burch, R. et al. (2002). "A review of the selective reduction of NO_x, with hydrocarbons under lean-burn conditions with non-zeolitic oxide and platinum group metal catalysts." Applied Catalysis B-Environmental 39(4): 283-303.

14. Burch, R. (2004). "Knowledge and know-how in emission control for mobile applications." Catalysis Reviews-Science and Engineering 46(3-4): 271-333.

15. United States Environmental protection Agency. Heavy-Duty Engines and Vehicles: Emission Standards Reference Guides. http://www.epa.gov/otaq /standards/ heavy-duty/index.htm. (Accessed Jul 6, 2013).

16. Hendershot, R. J. et al. (2003). "A novel reactor system for high throughput catalyst testing under realistic conditions." Applied Catalysis a-General 254(1): 107-120.

17. Devadas, M. (2006). "Selective Catalytic Reduction (SCR) of Nitrogen Oxides with Ammonia over Fe-ZSM5." Doctoral thesis, Swiss Federal Institute of Technology, Zurich.

18. Hendershot, R. J. (2005). "Multivariate and univariate analysis of infrared imaging data for high-throughput studies of NH_3 decomposition and NO_x storage and reduction catalysts." MEASUREMENT SCIENCE AND TECHNOLOGY 16: 302–308.

19. Hendershot, R. J. et al. (2003). "High-throughput catalytic science: Parallel analysis of transients in catalytic reactions." Angewandte Chemie-International Edition 42(10): 1152-1155.

20. Vijay, R. et al. (2006). "Performance of Co-containing NO_x storage and reduction catalysts as a function of cycling condition" Journal of Catalysis 243: 368–375.

21. Hendershot, R. J. et al. (2004). "Development and optimization of NO_x storage and reduction catalysts using statistically guided high-throughput experimentation." Catalysis Today 98(3): 375-385.

22. Hendershot, R. J. et al. (2006). "High-throughput study of the performance of NO_x storage and reduction catalysts as a function of cycling conditions and catalyst composition." Chemical Engineering Science 61(12): 3907-3916.

23. Fanson, P. T. et al. (2003). "FTIR analysis of storage behavior and sulfur tolerance in barium-based NO_x storage and reduction (NSR) catalysts." Applied Catalysis B-Environmental 46(2): 393-413.

24. Hendershot, R. J. et al. (2006). "High-throughput study of the influence of H_2O and CO_2 on the performance of nitrogen storage and reduction (NSR) catalysts." Applied Surface Science 252(7): 2588-2592.

25. Vijay, R. et al. (2005). "Noble metal free NO_x storage catalysts using cobalt discovered via high-throughput experimentation." Catalysis Communications 6(2): 167-171.

26. Hendershot, R. J. et al. (2007). "Response surface study of the performance of lean NO_x storage catalysts as a function of reaction conditions and catalyst composition." Applied Catalysis B-Environmental 70(1-4): 160-171.

27. Carucci, J. R. H. et al. (2009). "Kinetics of the biofuels-assisted SCR of NO_x over Ag/alumina-coated microchannels." Chemical Engineering Journal 154(1-3): 34-44.

28. Thomas, J. F. (2005). "Hydrocarbon Selective Catalytic Reduction Using a Silver-Alumina Catalyst with Light Alcohols and Other Reductants." SAE: 2005-01-1082.

29. Backman et al. (2006). "Kinetic considerations of H_2 assisted hydrocarbon selective catalytic reduction of NO over Ag/Al_2O_3 – II. Kinetic 81odeling." Applied Catalysis a-General 304(1): 86-92.

30. Ezike, R.C. (2011). "Bimetallic Silver Catalysts for the Reformate-Assisted Selective Catalytic Reduction of NO_x" Doctoral thesis, University of Michigan.

31. Breen, J. P. and Burch R. (2006). "A review of the effect of the addition of hydrogen in the selective catalytic reduction of NO_x with hydrocarbons on silver catalysts." Topics in Catalysis 39(1-2): 53-58.

32. Burch, R. et al. (1998). "Mechanistic considerations for the reduction of NO_x over Pt/Al_2O_3 and Al_2O_3 catalysts under lean-burn conditions." Catalysis Today 42(1-2): 13-23.

33. Burch, R. and Watling T. C. (1997). "Kinetics and mechanism of the reduction of NO by C_3H_8 over Pt/Al_2O_3 under lean-burn conditions." Journal of Catalysis 169(1): 45-54.

34. Burch, R. and Watling T.C. (1997). "The effect of promoters on Pt/Al_2O_3 catalysts for the reduction of NO by C_3H_6 under lean-burn conditions." Applied Catalysis B: Environmental 11: 207-216.

35. He, H. and Y. B. Yu (2005). "Selective catalytic reduction of NO_x over Ag/Al_2O_3 catalyst: from reaction mechanism to diesel engine test." Catalysis Today 100(1-2): 37-47.

36. Kameoka, S. et al. (1999). "Selective catalytic reduction of NO_x with CH_3OH, C_2H_5OH and C_3H_6 in the presence of O_2 over Ag/Al_2O_3 catalyst: Role of surface nitrate species." Physical Chemistry 2: 367-372.

37. Sumiya, S. (1997). "Reduction of lean NO_x by ethanol over Ag/Al_2O_3 catalysts in the presence of H_2O and SO_2" Catalysis Letters 50: 87-91.

38. Masuda, K. et al. (1996). "Silver-promoted catalyst for removal of nitrogen oxides from emission of diesel engines." Applied Catalysis B-Environmental 8(1): 33-40.

39. Meunier, F. C. et al. (1999). "Mechanistic aspects of the selective reduction of NO by propene over alumina and silver-alumina catalysts." Journal of Catalysis 187(2): 493-505.

40. Obuchi, A. et al. (1997). "A practical scale evaluation of catalysts for the selective reduction of NO, with organic substances using a diesel exhaust." Applied Catalysis B: Environmental 15: 37-47.

41. Wang, J. et al. (2005). "Novel $Ag-Pd/Al_2O_3-SiO_2$ for lean NO_x reduction by C_3H_6 with high tolerance of SO_2." Catalysis Communications 6(3): 195-200.

42. Angelidis, T. N. and Tzitzios V. (2003). "Promotion of the catalytic activity of a Ag/Al_2O_3 catalyst for the N_2O+CO reaction by the addition of Rh a comparative activity tests and kinetic study." Applied Catalysis B-Environmental 41(4): 357-370.

43. Morimune, et al. (1998). "Study of catalytic reduction of NO_x in exhaust gas from a diesel engine." Experimental Thermal and Fluid Science 18(3): 220-230.

44. Shimizu, K. I. and Satsuma, A. (2007). "Hydrogen assisted urea-SCR and NH_3-SCR with silver-alumina as highly active and SO_2-tolerant de-NO_x catalysis." Applied Catalysis B-Environmental 77(1-2): 202-205.

45. Shi, X. Y. et al. (2008). "Combination of biodiesel-ethanol-diesel fuel blend and SCR catalyst assembly to reduce emissions from a heavy-duty diesel engine." Journal of Environmental Sciences-China 20(2): 177-182.

46. Yu, Y. B. et al. (2004). "Mechanism of the selective catalytic reduction of NO_x by C_2H_5OH over Ag/Al_2O_3." Applied Catalysis B-Environmental 49(3): 159-171.

47. Forzatti, P. (2001). "Present status and perspectives in de-NO_x SCR catalysis." Applied Catalysis a-General 222(1-2): 221-236.

48. Forzatti, P. et al. (2010). "New "Enhanced NH3-SCR" Reaction for NO_x Emission Control." Industrial & Engineering Chemistry Research 49(21): 10386-10391.

49. Koebel, M. et al. (2000). "Urea-SCR: a promising technique to reduce NO_x emissions from automotive diesel engines." Catalysis Today 59(3-4): 335-345.

50. Deka, U. et al. (2012). "Confirmation of Isolated Cu^{2+} Ions in SSZ-13 Zeolite as Active Sites in NH_3-Selective Catalytic Reduction." Journal of Physical Chemistry C 116(7): 4809-4818.

51. Sluder, C. S. (2004). "Low Temperature Urea Decomposition and SCR Performance." SAE: 05FL-55 DRAFT.

52. Seker, E. et al. (2002). "NO reduction by urea under lean conditions over alumina supported catalysts." Applied Catalysis a-General 226(1-2): 183-192.

53. Fickel, D. W. et al. (2011). "The ammonia selective catalytic reduction activity of copper-exchanged small-pore zeolites." Applied Catalysis B-Environmental 102(3-4): 441-448.

54. Shimizu, K. I. and Satsuma, A. (2007). "Hydrogen assisted urea-SCR and NH$_3$-SCR with silver-alumina as highly active and SO$_2$-tolerant de-NO$_x$ catalysis." Applied Catalysis B-Environmental 77(1-2): 202-205.

55. Madia, G. et al. (2002). "Thermal stability of vanadia-tungsta-titania catalysts in the SCR process." Applied Catalysis B-Environmental 39(2): 181-190.

56. Alemany, L. J. et al. (1996). "Characterization and composition of commercial V2O5-WO3-TiO2 SCR catalysts." Applied Catalysis B-Environmental 10(4): 299-311.

57. Alemany, L. J. et al. (1995). "Reactivity and physicochemical characterization of V$_2$O$_5$-WO$_3$/TiO$_2$ DeNO$_x$ catalysts." Journal of Catalysis 155: 117-130.

58. Morimune, et al. (1998). "Study of catalytic reduction of NO$_x$ in exhaust gas from a diesel engine." Experimental Thermal and Fluid Science 18(3): 220-230.

59. Li, J. H. et al. (2011). "Low-temperature selective catalytic reduction of NO$_x$ with NH$_3$ over metal oxide and zeolite catalysts-A review." Catalysis Today 175(1): 147-156.

60. Berggrund, M. et al. (2009). "Influence of Synthesis Conditions for ZSM-5 on the Hydrothermal Stability of Cu-ZSM-5." Catalysis Letters 130(1-2): 79-85.

61. Sjovall, H. et al. (2006). "Selective catalytic reduction of NO$_x$ with NH$_3$ over Cu-ZSM-5 – The effect of changing the gas composition." Applied Catalysis B-Environmental 64(3-4): 180-188.

62. Grossale, A. et al. (2008). "Study of a Fe-zeolite-based system as NH3-SCR catalyst for diesel exhaust after treatment." Catalysis Today 136(1-2): 18-27.

63. Brandenberger, S. et al. (2011). "Hydrothermal deactivation of Fe-ZSM-5 catalysts for the selective catalytic reduction of NO with NH_3." Applied Catalysis B-Environmental 101(3-4): 649-659.

64. Rahkamaa-Tolonen, K. et al. (2005). "The effect of NO_2 on the activity of fresh and aged zeolite catalysts in the NH_3-SCR reaction." Catalysis Today 100(3-4): 217-222.

65. Kwak, J. H. et al. (2010) "Excellent activity and selectivity of Cu-SSZ-13 in the selective catalytic reduction of NO_x with NH_3." Journal of Catalysis 275(2): 187-190.

66. Kwak, J. H. et al. (2012) "Effects of hydrothermal aging on NH_3-SCR reaction over Cu/zeolites." Journal of Catalysis 287: 203-209.

67. Ma, L. et al. (2013) "Characterization of commercial Cu-SSZ-13 and Cu-SAPO-34 catalysts with hydrothermal treatment for NH_3-SCR of NO_x in diesel exhaust." Chemical Engineering Journal 225: 323-330.

68. Yang, X. F. et al. (2012) "Heterometal Incorporation in Metal-Exchanged Zeolites Enables Low-Temperature Catalytic Activity of NO_x Reduction." Journal of Physical Chemistry C 116(44): 23322-23331.

69. Hendershot, R. J. (2004) "Statistically guided High Throughput experimentation of NO_x storage and reduction catalysts" Doctoral Thesis, University of Delaware.

70. Technology Review: A Molecular Connection Reprint Vol 26 No2. "Toward Clean Technology: How High-Throughput Heterogeneous Catalysis helps"

http://naegeledesign.com/sndimage/magazine/reprints/Hetcatreprintb.pdf. (Accessed Oct 9, 2013).

71. Maier, W. F., K. Stowe, et al. (2007). "Combinatorial and high-throughput materials science." Angewandte Chemie-International Edition 46(32): 6016-6067.

72. Dar, Y. L. (2004). "High-throughput experimentation: A powerful enabling technology for the chemicals and materials industry." Macromolecular Rapid Communications 25(1): 34-47.

73. Snively, C. M. et al. (2001). "Chemically sensitive parallel analysis of combinatorial catalyst libraries." Catalysis Today 67(4): 357-368.

74. Snively, C. M. et al. (2001). "Parallel analysis of the reaction products from combinatorial catalyst libraries." Angewandte Chemie-International Edition 40(16): 3028-3030.

75. Snively, C. M. et al. (2000). "Chemically sensitive high throughput parallel analysis of solid phase supported library members." Journal of Combinatorial Chemistry 2(3): 243-245.

76. Snively, C. M. et al. (1999). "Fourier-transform infrared imaging using a rapid-scan spectrometer." Optics Letters 24(24): 1841-1843.

77. Elizabeth, M. D. (2011) "High Throughput investigation of supported catalysts for CO_x free hydrogen production from ammonia decomposition" Doctoral Thesis, University of Delaware.

78. Bedenbaugh, J. E. (2012) "Investigation of Catalytic Materials for cracking of Military Aviation fuel to Liquefied Petroleum Gas: High throughput Experimentation" Doctoral Thesis, University of Delaware.

79. Harmon, L (2003). "Experiment planning for combinatorial materials discovery." Journal of Materials Science, 38: 4479.

80. Maxwell, IE, et al. (2003). "High-throughput technologies to enhance innovation in catalysis." Topics in Catalysis, 24: 125.

81. Senkan, S. (2001). "Combinatorial Heterogeneous Catalysis – A New Path in an Old Field." Angewandte Chemie International Edition, 40: 312.

82. Kramer, R. (1998). "Chemometric Techniques for Quantitative Analysis." Marcel Dekker INC., New York, NY10016.

83. Thermo Scientific GRAMS Suite Help.

84. Campanati, M. et al. (2003). "Fundamentals in the preparation of heterogeneous catalysts" Catalysis Today 77: 299-314.

85. Bings, N. H. et al. (2010) "Atomic Spectroscopy: A Review" Analytical Chemistry 82: 4653-4681.

86. Radislav, A. P. et al. (2003). "High-throughput Analysis A Tool for Combinatorial Material Science." Kluwer Academic/Plenum Publishers, New York.

APPENDIX A – Data Collection and preliminary processing

Data is collected by using WinIR and preliminary processing of data is done by JAIMP designed in-house. In OPUS, the spectral resolution, interferometer mirror speed, and the total number of data points collected per interferograms are interrelated. So, all parameters were adjusted simultaneously. The sample scan time and background scan time is set to very high numbers, so that the spectrometer does not go into idle mode in the middle of data collection, which might manifest as a shift in the interferogram.

In the WinIR gain determines the signal to noise ratio. Gain is chosen as 0 (zero) to minimize the signal to noise ratio. The intensity of the interferogram as shown in Figure-A.1 is determined by integration time and offset: higher the integration time higher the intensity. However, the integration time should not be high enough to saturate the detector. In video save section 32grabs and 1920 frames to capture per grab are chosen to utilize the maximum frame grabbing capacity of the FPA detector and to get a file of 61440 frames.
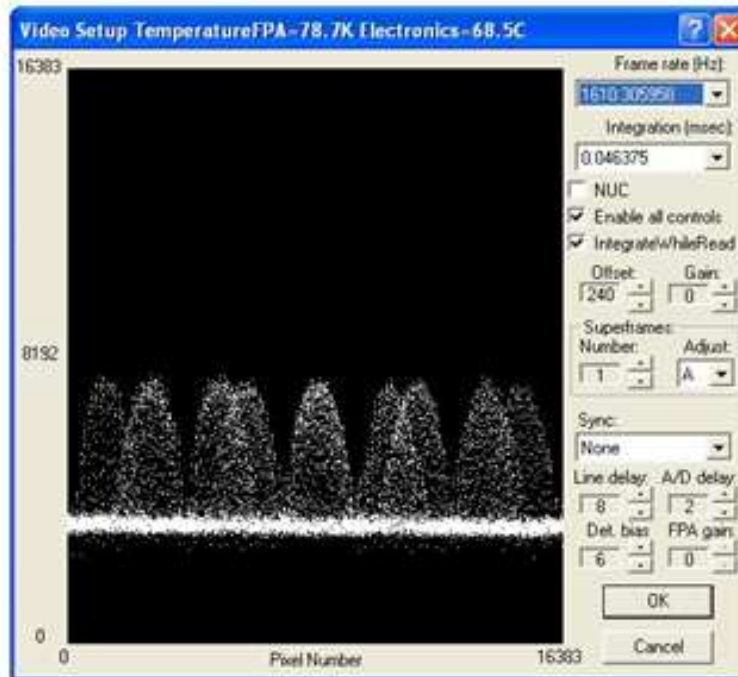
Figure-A.1: Intensity of the interferogram in WinIR.

The data collected by WinIR is an image (.img) file. This file is preprocessed using JAIMP to get rid of the bad pixels, resulting a reduced size of image (.ppimg) file. The bad pixels that do not contain interferograms are those blocked by the 316 grade stainless steel plates compressing the ZnSe windows to the GPA tubes. Therefore, the only regions in the images with true interferograms are those associated with the GPA tubes. This file is then separated to 32 interferogram files by JAIMP to remove the bad interferograms based on the shift of the interferogram from the center as shown in Figure-A.2.
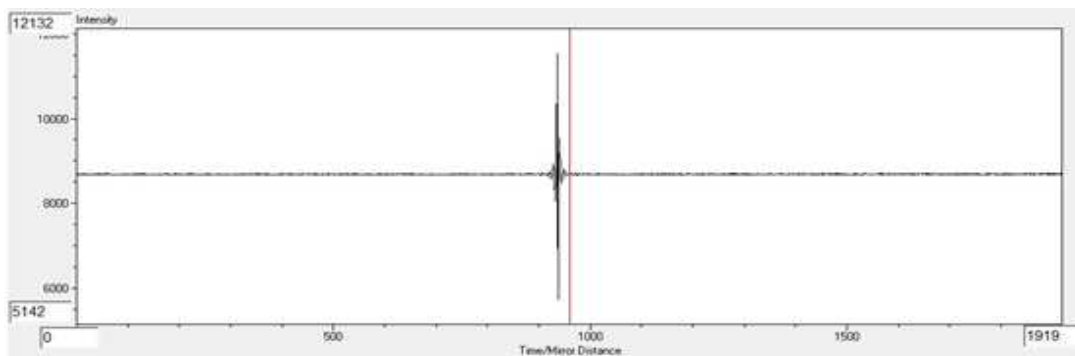
Figure-A.2: Shift of the interferogram from the center.

The good interferograms are Fourier transformed and coadded in JAIMP to get the transmittance spectra. Background transmittance spectra are collected by flowing only N_2 through the GPA, while other transmittance spectra are collected by flowing different gas mixtures through GPA. The absorbance spectra are obtained by taking the ratio of any transmittance spectra to the background. As shown in Figure-A.3 the usable wavenumber range is ~ 4000-900cm^{-1}.
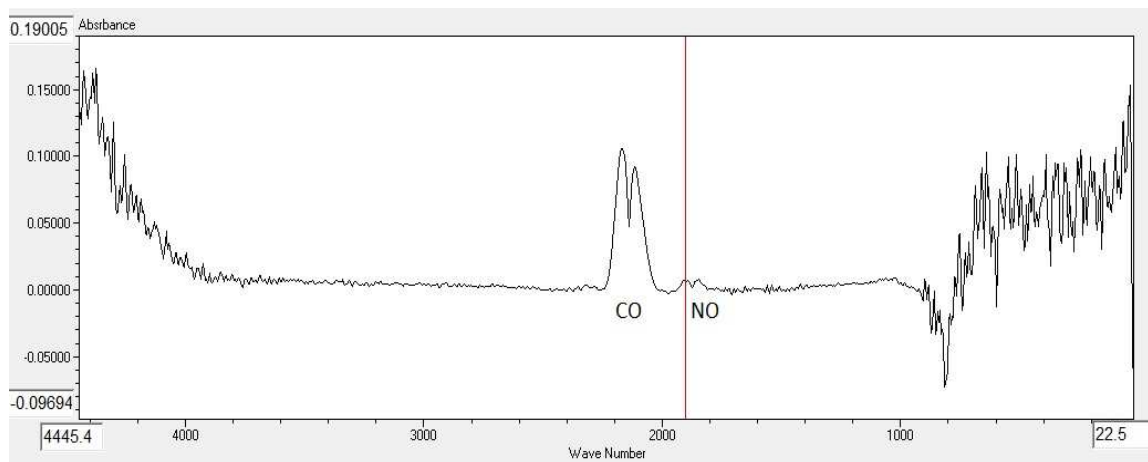

Figure-A.3: The absorbance spectra of NO and CO.

A mask (.msk) file is prepared in JAIMP to specify the position of each channel of the GPA in pixels. Using the mask file and wavenumber range of a peak, the area of the peak can be calculated. The mask is also used to transform the absorbance spectra to spectroscopic data (.spc) file which can be read by GRAMS.

A wavenumber calibration is necessary to match the frame numbers with the wave numbers. This was done by using absorbance spectra of NO, CO and CO_2. The frame numbers corresponding to the peaks were read from JAIMP and the corresponding wave numbers were taken from National institute of Standard and Technology (NIST) chemistry web book. The calibration is shown in Figure-B.1. The calibration determines the left and right wavenumber in the x axis of JAIMP.
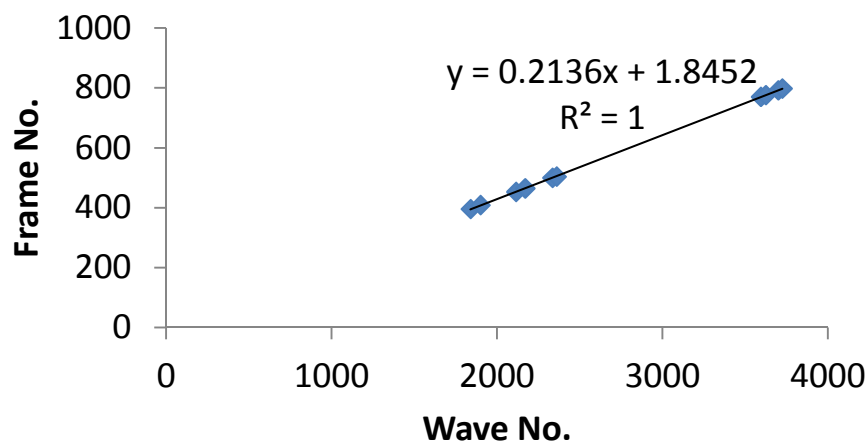

Figure-B.1: Wavenumber calibration.